Characterization and Modeling of Grain Boundary Chemistry Evolution in Ferritic Steels under Irradiation

Nuclear Energy Advanced Modeling and Simulation

Emmanuelle Marquis
University of Michigan

In collaboration with:
University of Tennessee

Sue Lesica, Federal POC
Di Yun, Technical POC

NEUP | Nuclear Energy University Programs

U.S. Department of Energy

Characterization and Modeling of Grain Boundary Chemistry Evolution in Ferritic Steels under Irradiation

NEUP Project # 11-3033

FINAL REPORT

PI
Emmanuelle A Marquis
University of Michigan
(734) 764-8717
emarq@umich.edu

Co-PIs

Brian Wirth
University of Tennessee
(865) 974-2554
bdwirth@utk.edu

Gary Was
University of Michigan
(734) 763-4675
gsw@umich.edu

Collaborator
G. Robert Odette, Peter Wells
University of California, Santa Barbara

Masters Students
Reshma Mathew, University of Michigan
Aaron Selby, University of Tennessee

Post-docs
Lan Yao, University of Michigan
Mukesh Bachhav, University of Michigan
Ben Ramirez, University of Tennessee

1. Summary

Ferritic/martensitic (FM) steels such as HT-9, T-91 and NF12 with chromium concentrations in the range of 9-12 at.% Cr and high Cr ferritic steels (oxide dispersion strengthened steels with 12-18% Cr) are receiving increasing attention for advanced nuclear applications, e.g. cladding and duct materials for sodium fast reactors, pressure vessels in Generation IV reactors and first wall structures in fusion reactors, thanks to their advantages over austenitic alloys. Predicting the behavior of these alloys under radiation is an essential step towards the use of these alloys. Several radiation-induced phenomena need to be taken into account, including phase separation, solute clustering, and radiation-induced segregation or depletion (RIS) to point defect sinks.

RIS at grain boundaries has raised significant interest because of its role in irradiation assisted stress corrosion cracking (IASCC) and corrosion of structural materials. Numerous observations of RIS have been reported on austenitic stainless steels where it is generally found that Cr depletes at grain boundaries, consistently with Cr atoms being oversized in the fcc Fe matrix. While FM and ferritic steels are also subject to RIS at grain boundaries, unlike austenitic steels, the behavior of Cr is less clear with significant scatter and no clear dependency on irradiation condition or alloy type. In addition to the lack of conclusive experimental evidence regarding RIS in F-M alloys, there have been relatively few efforts at modeling RIS behavior in these alloys. The need for predictability of materials behavior and mitigation routes for IASCC requires elucidating the origin of the variable Cr behavior.

A systematic detailed high-resolution structural and chemical characterization approach was applied to ion-implanted and neutron-irradiated model Fe-Cr alloys containing from 3 to 18 at.% Cr. Atom probe tomography analyses of the microstructures revealed slight Cr clustering and segregation to dislocations and grain boundaries in the ion-irradiated alloys. More significant segregation was observed in the neutron irradiated alloys. For the more concentrated alloys, irradiation did not affect existing Cr segregation to grain boundaries and segregation to dislocation loops was not observed perhaps due to a change in the dislocation loop structure with increasing Cr concentration. Precipitation of α' was observed in the neutron irradiated alloys containing over 9 at.% Cr. However ion irradiation appears to suppress the precipitation process. Initial low dose ion irradiation experiments strongly suggest a cascade recoil effect. The systematic analysis of grain boundary orientation on Cr segregation was significantly challenged by carbon contamination during ion irradiation or by existing carbon and therefore carbide formation at grain boundaries (sensitization).

The combination of the proposed systematic experimental approach with atomistic modeling of diffusion processes directly addresses the programmatic need for developing and benchmarking predictive models for material degradation taking into account atomistic kinetics parameters.

Table of Content

2. Introduction

Ferritic-martensitic (F-M) steels such as HT-9, T-91 and NF12 with chromium concentrations in the range of 9-12 at.% Cr and high Cr ferritic steels (oxide dispersion strengthened steels with 12-18% Cr) are receiving increasing attention for advanced nuclear applications, e.g. cladding and duct materials for sodium fast reactors, pressure vessels in Generation IV reactors and blanket structures in fusion reactors, thanks to their advantages over austenitic alloys. They exhibit limited thermal expansion, high thermal fatigue resistance, and higher resistance to void swelling [2, 3] as compared to austenitic steels. Several thermal and radiation-induced phenomena can affect the microstructure of these alloys and grain boundary properties in particular. Predicting the behavior of these alloys under radiation is therefore an essential step towards their safe long-term use.

Depending on heat-treatment conditions, quenching rates, and the presence of minor elements, either segregation or depletion of Cr is observed in annealed ferritic and ferritic-martensitic alloys. Cr segregation has been reported after tempering at temperatures between 450-1060°C [4]. The formation of Cr-rich carbides below 700°C can lead to the depletion of Cr at grain boundaries (sensitization effect) [5, 6], which has been linked to grain boundary embrittlement. In the higher Cr ferritic steels (>14at.%), the precipitation of the α' phase during thermal anneal has also been linked to embrittlement (the 475°C effect) [7]. Besides microstructural changes related to thermal annealing, neutron irradiation can also induce a change of microstructure (point defect clusters, dislocation network, precipitates) and microchemistry (segregation of alloying elements and impurities at sinks, e.g. grain boundaries). These changes result in the degradation of mechanical properties of structural materials, such as radiation-induced hardening and embrittlement. In particular, radiation-induced segregation or depletion (RIS) at grain boundaries has raised significant interest because of its role in irradiation assisted stress corrosion cracking (IASCC) of austenitic steels and corrosion of structural materials [8].

2.1. Cr precipitation

The Fe-Cr phase diagram exhibits a miscibility gap between the Fe-rich phase (α) and the Cr-rich phase (α') which contains over 90 at.% Cr [9]. Determining the solubility of Cr in α-Fe has generated a lot of interest from the experimental and theoretical community, e.g. [10-13], the motivation being that the possible formation of α' during irradiation can lead to significant hardening and therefore embrittlement of ferritic and ferritic martensitic steels with Cr concentrations over ~10% [7]. However, the understanding of α' formation is not thorough enough to provide quantitative predictions. In particular, alloy chemistry, the effect of common impurities such as Si, C, or P, and conditions under which α' forms are not fully defined. Yet, such an understanding is important for appropriately selecting alloys for nuclear reactor parts and for predicting the evolution of their properties under irradiation.

Cr is an extremely slow diffuser in α-Fe [14, 15], precluding thermal studies to be performed easily. On the other hand, irradiation can provides a mean to accelerate diffusion and therefore the precipitation kinetics of because of the increase concentration of point defects, however a number of limitations can arise as reviewed in details in Ref. [16]. Particularly, ballistic dissolution competing with the thermodynamic driving force can lead to precipitate dissolution and therefore an apparent increase in solubility.

The phase α' has been observed in a large number of studies on neutron irradiated steels, both model and commercial alloys. Typically α' forms in alloy containing at least 8.5%Cr with diameters varying from 1.2 nm after irradiation at 325 °C and 0.7 dpa [17] to 8-10nm at 425 °C and 26 dpa [18]. Precipitate free zones were observed around voids [19] and grain boundaries [20]. Measurement of the matrix compositions points to a steady-state Cr solubility of about 9 at.% Cr for neutron irradiation at 300 °C [21].

In the case of proton irradiated alloys, Kuwano reported α′ forming in alloys containing more than 9 at.% Cr, even for irradiation temperature of -60 $^{\text{o}}$C [22]. Jiao reported Cr rich clusters without specifying the composition in HT9 and HCM12 irradiated at 400 $^{\text{o}}$C to 7 dpa [23]. Their appearance of the APT reconstructions however suggest the α′ phase.

No convincing report of α′ formation during ion irradiation could be found. A couple of reports mention the presence of carbon and chromium clusters [24] or Cr clustering within dislocation loops [25]. Kai [26] hypothesized the presence of 5nm α′ precipitates in ion irradiated HT9 at 400 $^{\text{o}}$C, associated with dislocation loops and a non-uniform distribution. However no chemical or structural analysis was done. Borodin [27] mentioned the presence of α′ in 13Cr-2Mo ion irradiated at 250-425 $^{\text{o}}$C, without providing any experimental evidence. Hardie [24] performed lower dose rate experiments and reported Cr and N-rich features with up to 15-10 at.% Cr in lower rate ion irradiation at 3 x 10^{-5} dpa/s. Again no α′ was observed which is not surprising considering the relatively low Cr content of the alloy.

Whether α′ forms in Fe-Cr alloys under ion irradiation remain an open question.

2.2. Grain boundary chemistry

Numerous observations of RIS on austenitic stainless steels have been reported and generally found that Cr depletes at grain boundaries, consistently with the fact that oversized Cr atoms preferentially bind with vacancies and diffuse faster in the FCC Fe matrix. While F-M and ferritic steels are also subject to RIS at grain boundaries, unlike austenitic steels, the behavior of Cr is less clear. The available literature contains significant scatter and no clear dependency on irradiation condition or alloy type, and indeed grain boundary Cr segregation, Cr depletion, as well as no compositional changes have been reported in various studies, e.g. [3, 28-35]. Unfortunately, the irradiation conditions (alloy, dose, dose rate, temperature, irradiating ion) are so varied among the few data points that there were essentially no two data points taken under the same irradiation conditions. The lack of a systematic study makes it impossible to draw any conclusions about the behavior of Cr under irradiation. The need for predictability of materials behavior in the long term and mitigation routes for IASCC requires elucidating the origin of the variable Cr behavior.

Both Auger electron spectroscopy (AES) and scanning transmission electron microscopy (STEM) with electron dispersive x-ray spectroscopy (EDXS) have been the techniques of choice for studying grain boundary chemistry. However, AES lacks lateral spatial resolution, and its depth resolution is limited by the complexity of the associated ion sputtering process and the range of electron penetration and escape depths. STEM-EDXS provides chemical profiles across grain boundaries at high resolution (e.g. [36]). However, it does not provide reliable information on impurity levels and on the solute distribution within the grain boundary planes. Atom-probe tomography (APT) has made major contributions to the understanding of segregation processes, both because of its high spatial and chemical resolution, single-atom detection capability, and because it does not require the specimen to be fractured prior to examination. The role of grain boundary character and presence of solutes on Cr segregation or depletion during irradiation will therefore be extensively studied using APT in combination with orientation imaging, focused ion beam (FIB) milling, TEM, EDXS and electron energy loss spectroscopy (EELS).

2.3. Work scope

A combination of controlled heavy ion irradiations, detailed high-resolution structural and chemical characterization, and atomistic modeling will be used to answer the following questions:
- What are the conditions leading to α′ precipitation?
- How does grain boundary character influence Cr (and minor alloying element) RIS behavior?
- How does the presence of C influence RIS of Cr?
- What is the effect of Cr concentration on diffusion and grain boundary chemistry?

- Will interstitial-mediated transport indeed produce Cr enrichment, and can a combination of faster Cr diffusion by both vacancy and interstitial-mediated diffusion mechanisms explain the complex Cr RIS behavior observed?
- Do the trends observed in ion irradiation studies hold for neutron irradiation?
- Can we validate models of Cr RIS in ion and neutron irradiation laboratory based studies that are extrapolated to advanced reactor operating conditions?

3. Materials

3.1. Materials for ion irradiation

The alloys used in this study are high purity Fe-Cr alloys of varying chromium concentration of 5, 10 and 14 wt% that were supplied by the EFDA (European Fusion Development Agreement). The preparation of these alloys consisted of induction melting in a cold crucible using high purity hydrogen and argon in order to eliminate carbon, nitrogen, sulphur and oxygen. The final compositions were measured by Glow Discharge Mass Spectrometry (GDMS) and are shown in **Table 1**.

Table 1: Impurity contents in the three Fe-Cr alloys used for the ion irradiation.

Alloy	C wt ppm	S wt ppm	O wt ppm	N wt ppm	P wt ppm
Fe 5%Cr	3/4	3/3	4/6	3/2	<5
Fe 10%Cr	4/4	6/4	3/4	3/3	<5
Fe 14%Cr	4/5	6/7	4/4	5/5	<10

3.2. Materials for neutron irradiation

The six Fe-Cr alloys used in this study was originally investigated by Gelles et al. in the 1980s as part of the fast breeder reactor program [37, 38]. A cold rolled sheet condition of this alloy was annealed under an argon atmosphere at 950°C for 15 minutes followed by air cooling, then re-annealed at 750°C for 1 h, again followed by air cooling. This resulted in an equiaxed and recovered structure with a relatively large grain size of the order 50-100 μm, and a low dislocation density as indicated by low hardness values.

The matrix compositions measured by atom probe tomography from analyses performed away from grain boundaries are shown in **Table 2.** The values obtained are in good agreement with the expected compositions for Cr and reveal the presence of Ni, Si, P, Mn, C, and V as impurities.

Table 2: Compositions of the six Fe-Cr alloys used for the ion irradiations (in at.%).

Alloy	Cr	Ni	Si	P	Mn	C	V
Fe-3Cr	2.9	0.12	0.03	.01	0.02	0.08	0.01
Fe-6Cr	5.8	0.03	0.05	0.01	0.01	0.03	0.01
Fe-9Cr	9.3	0.01	0.05	0.01	0.01	0.01	0.02
Fe-12Cr	11.4	0.02	0.05	0.01	0.01	0.01	0.01
Fe-15Cr	15.1	0.02	0.04	0.01	0.02	0.02	0.01
Fe-18Cr	18.4	0.01	0.07	0.01	0.02	0.03	0.02

4. Irradiations

4.1. Ion irradiation

Ion irradiation using 5 MeV Fe^{++} ions was performed using the Tandem accelerator in the University of Michigan. The specimens were mounted on a copper stage with a 0.1 μm thick indium foil used as the coolant. Guide bars were mounted on either side of the specimens and they were all held in place by hold-down bars. Thermocouples were attached to the guide bars to keep track of the temperature before the irradiation starts. Four independent apertures are used to define the irradiated portion of the samples and to center the scanned beam. The sample temperature is controlled using a cartridge heater mounted in the sample stage block. Air flows through a series of cooling coils in the sample block and maximum control of the sample temperature is achieved by controlling both heating and cooling. The sample is also heated by the energy deposited by the beam. However, at 400-600 ℃, 5 MeV Fe^{++} ions provide an increase of only ~5℃ to the sample temperature according to previous experience. Therefore, heating by the heavy-ion beam is insignificant. Control of the sample temperature is achieved by using a liquid indium layer between the stage and the samples to provide a high thermal conductivity path to the stage block. Sample temperature is measured using a high resolution, 2D thermal imager.
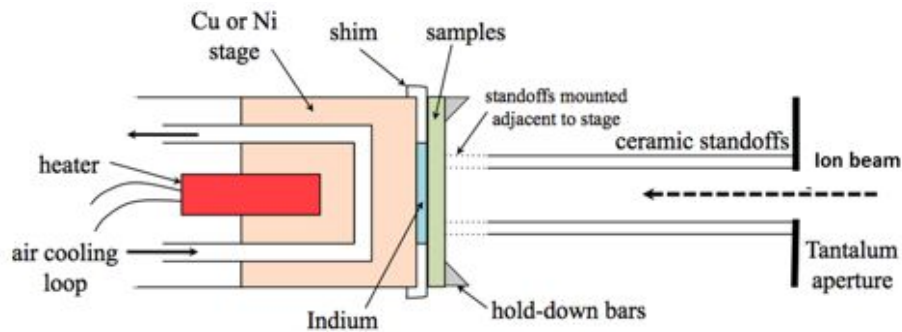
Figure 1: Schematic of the stage being irradiated. From [39]
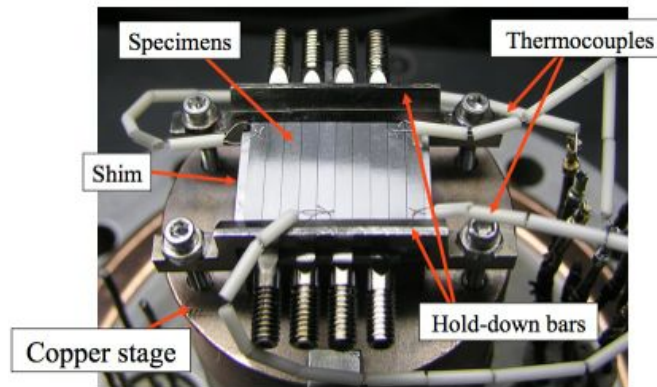
**Figure 2**: Illustration of the specimen stage with thermocouples attached. From [39]

Once the irradiation was completed, the specimens were carefully removed from the stage and cleaned with distilled water and dried using a jet of dry compressed air.

Specimens were implanted using 5 MeV Fe^{++} ions to various doses ranging from a low (1dpa) to a high dose (60 dpa) at an average dose rate of 10^{-3} ± 50% dpa/s at temperatures ranging from 300 °C to 500 °C ± 10°C. The details of alloys implanted are given in **Table 3**.

Table 3: irradiation conditions

Dose	1 dpa	10 dpa	60 dpa
Temperature			
300°C ± 10°C	5, 10, 14Cr	5, 10, 14Cr	5, 10, 14Cr
500°C ± 10°C	5, 14Cr	5, 14Cr	-

Both the dose and dose rate for Fe^{++} irradiation were calculated using the SRIM code [40] using a threshold energy for Fe of 53 eV [41]. The damage is measured in terms of the number of vacancy-interstitial pairs produced in the material. The expected damage profile is illustrated in **Figure 3**. Traditionally, microstructural investigations have been performed at a depth of 500-700 nm from the irradiated surface. This "analysis" depth is selected to avoid: 1) an alteration in the alloy composition by the irradiating particle, and 2) the injected interstitial effect that is known to suppress swelling [42]. At ~500 nm depth, the effect of both are negligible. However, this does not exclude surface effects, microstructural inhomogeneity, or possible errors in case of a strong depth dependence. Selecting this particular depth as representative may limit the range of our observations gained from such involved irradiation experiments. Instead, our approach and results focusing on probing the full depth analysis from the implanted surface to a depth beyond 2 µm highlight the available data. Our results also raise questions regarding the representative character of isolated analyses in the context of such microstructural complexity.
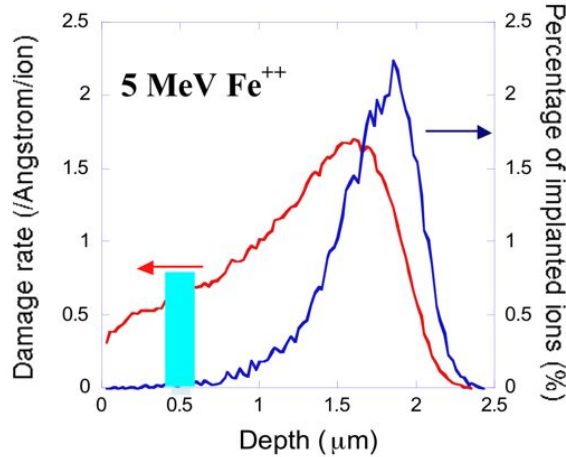
Figure 3: Damage and irradiation profiles for 5 MeV Fe^{++} irradiation of steel. The traditionally chosen analysis depth, shown by the blue stripe, avoids the implanted ion, the peak damage region and the surface.

4.2. Neutron irradiation

Irradiations had been carried out in the Advance Test Reactor (ATR) at Idaho National Laboratory within the ATR program led by Prof. G. Robert Odette at UCSB. The series of six Fe-Cr alloys of nominal compositions 3, 6, 9, 12, 15, and 18 at.% Cr were irradiated at a neutron fluence (E>1 MeV) of 1.1×10^{21} n/cm^2 at 563 ± 15 K and to a damage level of 1.82 dpa. Nominal neutron flux and dpa rate are 2.3×10^{14} n/cm^2/s and 3.4×10^{-7} dpa/s respectively.

5. Characterization

5.1. Metallography

After each stage of polishing (from 320, 600 and 800 grit to 9 µm, 6 µm, 3 µm and 1 µm), the alloys were thoroughly ultrasonically cleaned using only distilled water. The alloys were dried using streams of dry compressed air. For the last stage of the specimen preparation, the alloys were removed from the polishing mount and the crystal glue on the back face of the alloys was cleaned carefully using acetone without affecting the polished face. Finally, the specimens were electropolished in a solution of 5% perchloric acid in methanol cooled to -50 °C using dry ice in order to get a nice clean surface free of contaminants and to remove the mechanical damage introduced by manual polishing.

5.2. Atom probe tomography (APT)

The combination of electron back-scattered diffraction (EBSD) for orientation imaging, focused ion beam (FIB) milling, and APT is used to systematically investigate the relationship between misorientation, plane, structure and chemistry of grain boundaries, as illustrated in **figure 4**. EBSD provides grain boundary orientation mapping allowing the selection of grain boundaries of specific character (low sigma, low angle, high angle, etc.).
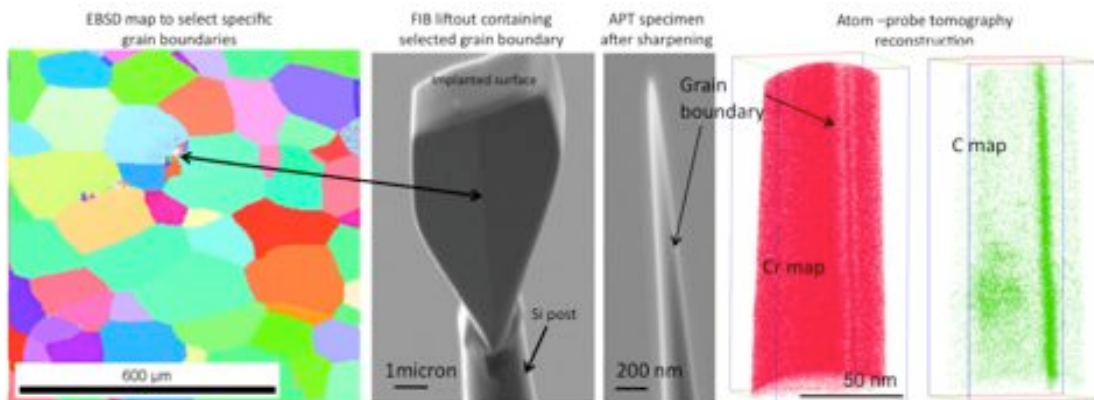

Figure 4: EBSD, FIB specimen preparation, APT reconstruction of Cr and C in specimens containing a selected grain boundary.

5.2.1. Specimens and full depth analysis

Specimens were prepared by focused ion beam milling and a standard liftout process [43] using either a FEI dual beam SEM Quanta 3D 200i at CAES, INL or a FEI dual beam SEM Nova 200 Nanolab and Helios 650 Nanolab at the Michigan Center for Materials Characterization. The steps required for the preparation are illustrated in **Figure 5** and include Pt deposition over the region of interest, milling of trenches to form a 20 to 30 um by 3 um beam with a triangular cross-section, lifting of the beam using a Pt micro-manipulator and deposition of the beam onto Si post so as to create 5 to 8 specimens. **Figure 6** illustrates the annular milling process to create needle-shaped specimens with end radii < 100 nm.

The FIB lift-out process enables control of the depth at which the needles are extracted. Furthermore the annular milling steps offers additional control to position the apex of the samples at a desired depth. We therefore developed a method to analyze the full implanted depth and into the pristine region. This

complete analysis allows probing of potential surface effects, a potential dependence with dose of the microstructure. In addition, it offers an avenue to understand microstructural variations and a background for interpreting the APT data based on very small volumes.
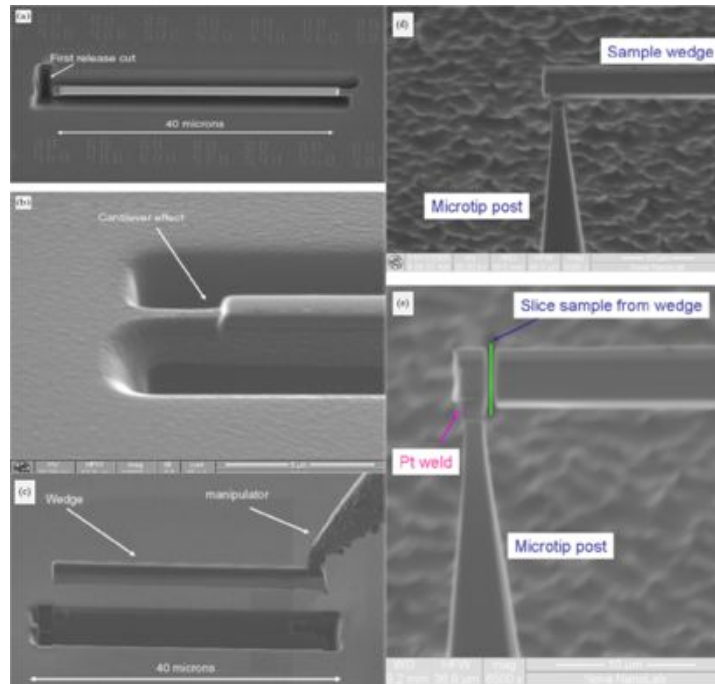
Figure 5: Illustration of the APT specimen preparation steps
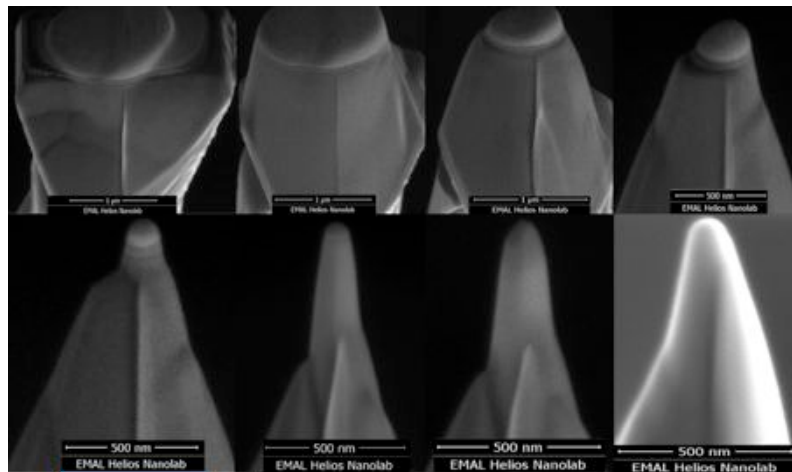
Figure 6: Annular milling to create needle-shaped specimens

5.2.2. Data collection

A LEAP 4000X HR instrument was used for atom probe tomography data collection. Specimens were cooled to a base temperature of 50 to 55 K and analyzed in either voltage pulsing mode (with a pulse fraction of 20%) or laser mode (energy in the range of 30-60 pJ/pulse). The pulse repetition rate was set at 200 KHz, and a constant detection rate in the range of 0.003-0.005 atoms/pulse was used during data

collection. Voltage mode was the preferred mode of operation. However in the case of fragile specimens, laser was used.

5.2.3. Data reconstruction

Data reconstruction and analysis was performed using the Cameca Visualization and Analysis Software (IVAS 3.6.6). Standard parameters for the average evaporation field (33V/nm) and the detector efficiency (0.36) were used for reconstruction of the datasets. The image compression factor and k-factor were adjusted based on identified poles and plane spacing, radial density, or tip geometry such as initial radius and shank angle obtained from SEM images during FIB milling.

## 5.3. On the evaporation behavior and analysis of grain boundaries

APT offers unique opportunity to access atom-by-atom information with very high chemical and spatial resolution that no other technique can match. However, challenge remains for multi-component materials and interfaces in terms of chemical and spatial resolution. For instance, the so-called local magnification effect is a well-known artifact arising due to difference in evaporation field of different phases leading to slight deviation of atoms from their original site in the material [44]. It is now well established that aberrations of ion trajectories and local magnification effects control the spatial resolution in APT. A few studies have been performed to understand the effects of varying evaporation fields on 3D reconstruction of microstructures containing small clusters or multi-layers [45].

It is conceivable that the same evaporation artefacts affect the analysis of grain boundaries. Therefore, accurate 3D reconstruction from grain boundaries by APT requires a detailed understanding of the evaporation behavior and the effects on solute positioning.

We first addressed this question by investigating the evaporation behavior of a $\Sigma 3$ grain boundary in a simple binary system Fe-15Cr alloy both experimentally and theoretically. A $\Sigma 3$ boundary is first found by Electron Backscatter Diffraction (EBSD) analysis. APT specimens containing the very same boundary are then prepared by focused ion beam (FIB) milling and lift-out in such as way that the boundary is positioned at different angles with respect to the axes of needle-shaped APT specimens. SEM images and 3-D reconstructions of specimens with the grain boundary at two different orientations (parallel and perpendicular with respect to tip axis) are shown in **Figures 7 & 8**, respectively. 1-D concentration profiles of Cr atom taken perpendicular to the grain boundary for both orientations reveal clear that orientation within the samples strongly affect the measure segregation profile. Not surprisingly, the horizontal configuration leads to the best spatial accuracy. This experiment illustrate why reporting the segregation peak is not a valid measure of segregation, rather the Gibbsian excess which counts the excess number of Cr atoms around the grain boundary is the relevant measure. The values are comparable for the two cases presented here.
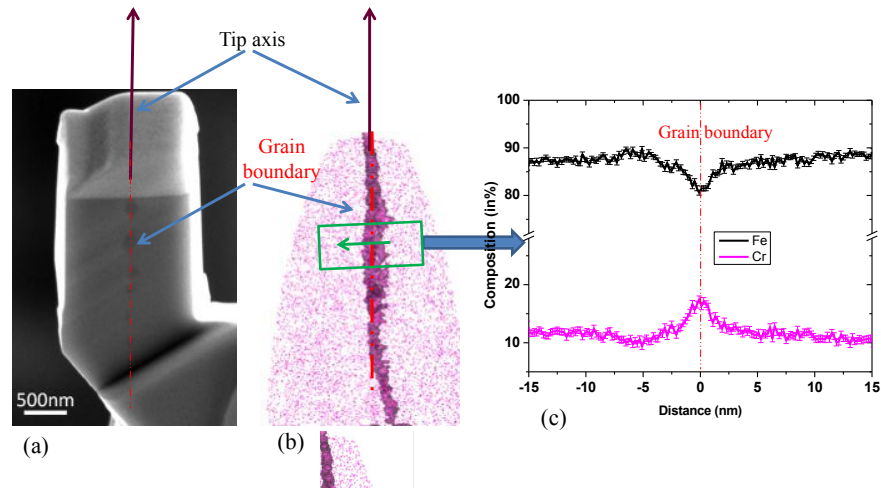
Figure 7. Grain boundary parallel to tip axis: (a) SEM image of lift-out (b) Reconstructed volume analyzed by APT showing Cr segregation and (c) 1 D profile of Fe and Cr atoms across grain boundary.
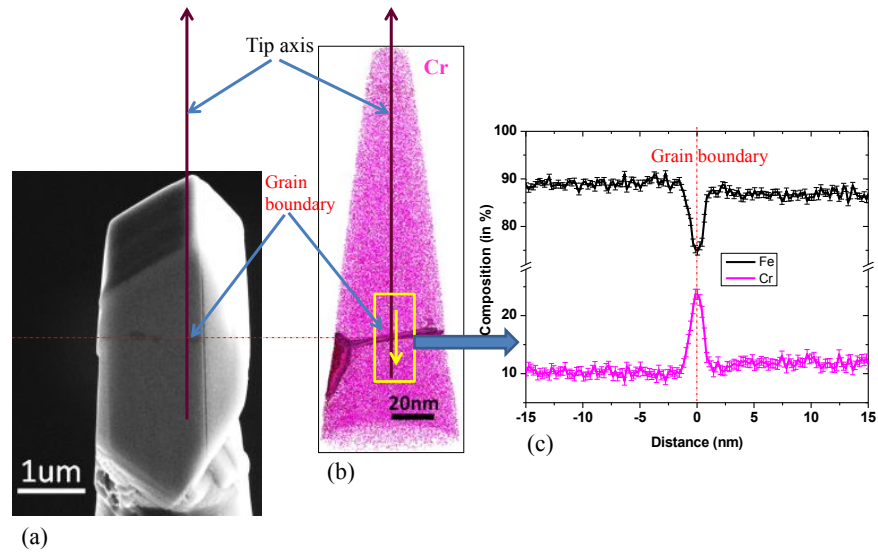
Figure 8. Grain boundary perpendicular to tip axis: (a) SEM image of lift-out (b) Reconstructed volume analyzed by APT showing Cr segregation and (c) 1 D profile of Fe and Cr atoms across grain boundary.

6. Microstructures after ion irradiation

6.1. Matrix (Away from grain boundaries)

No α' phase was observed for any of the conditions, even in the higher Cr containing alloy. Instead small Cr clusters were noted, preferentially formed on dislocation loops and associated with C segregation. The Cr concentration in these clusters was measured between 30 and 50 at.% Cr, far from the concentrations > 85 at.% Cr measured in the α' precipitates formed during neutron irradiation. These results suggest a strong dose rate effect, which is being investigated through lower dose rate ion irradiation in the temperature range of 300 to 600 ^{o}C to map the conditions under which α' forms.

6.1.1. Irradiation at 300 ^{o}C

In the Fe-10 at.% Cr alloy irradiated to 10 and 60 dpa, few Cr clusters were found with concentration ~ 30 at.% Cr. Some of the clusters may be forming along dislocation lines, as suggested by their elongated shape (**Figure 9 left**). Others, significantly smaller exhibit a spherical shape (**Figure 9 right**).
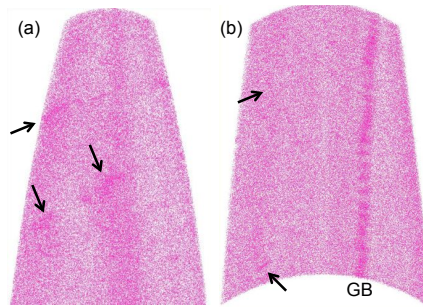
Figure 9: Slices through the Fe-10 at.% Cr alloy irradiated at 300 ^{o}C to 1 and (a) 10 and (b) 60 dpa.

In the Fe-15 at.% Cr alloy also irradiated to 10 dpa, the clusters are even more very difficult to observe, being smaller than any of the other conditions and alloys (**figure 10**). The number density of clusters also appears to be much higher than in any of the other alloy conditions.
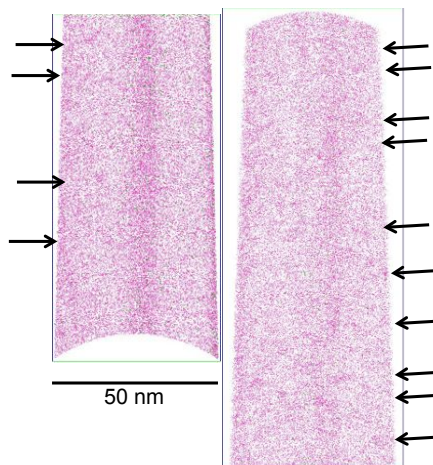
Figure 10: Slices through the Fe-15 at.% Cr alloy irradiated at 300 ^{o}C to 1 and 10 dpa.

6.1.2.irradiation at 500 ^{o}C – 1 dpa

The Fe-5 at.% Cr alloy exhibits very clear Cr precipitates distributed non-uniformly with tendency to form in preferential locations (**figure 11**). The composition of the clusters as determined by the proximy histogram method is 18 at.% Cr with ~1 at.% C. Some of the cluster groups form planar features, with a habit plane of (100), suggesting that the Cr clusters appear to decorate the center of <100> dislocation loops. Some of the Cr clusters appears to form loop patterns, some of which have a (100) or a (110) habit plane. The loop size is consistent with a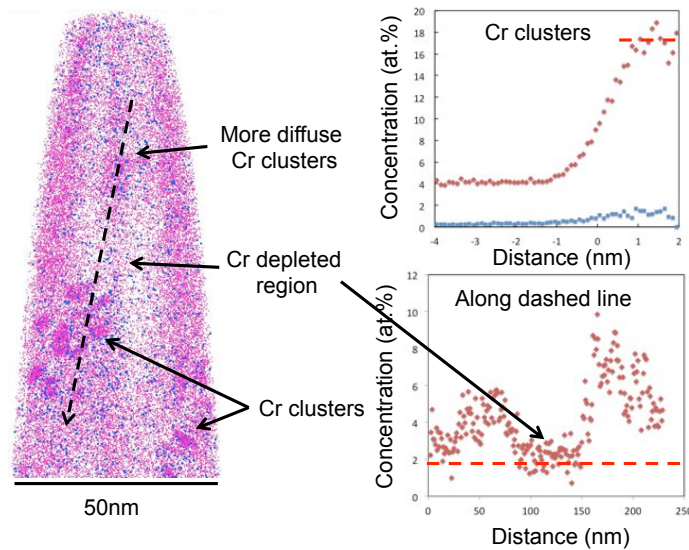 range of 50 nm and upwards. Large regions depleted in Cr (~2 at.% compared to the alloy concentration of 5%) can also be seen around these dislocations.

Figure 11: Fe-5 at.% Cr alloy irradiated at 500 ^{o}C to 1 dpa

In the Fe-15 at.% Cr alloy, the spatial distribution of Cr suggest very small spherical or rod-like clusters with Cr concentration about 30 at.% Cr, and larger Cr clusters with concentration of 30 to 45 at.% Cr and 1 to 3 at.% C (**Figure 12**). Thin particles with similar Cr and C concentrations are observed along grain boundaries. We note that no α′ phase is observed at grain boundaries. It is still unclear whether Cr clustering occurs inside dislocation loops as it was observed for the 5Cr alloy or along dislocation lines.
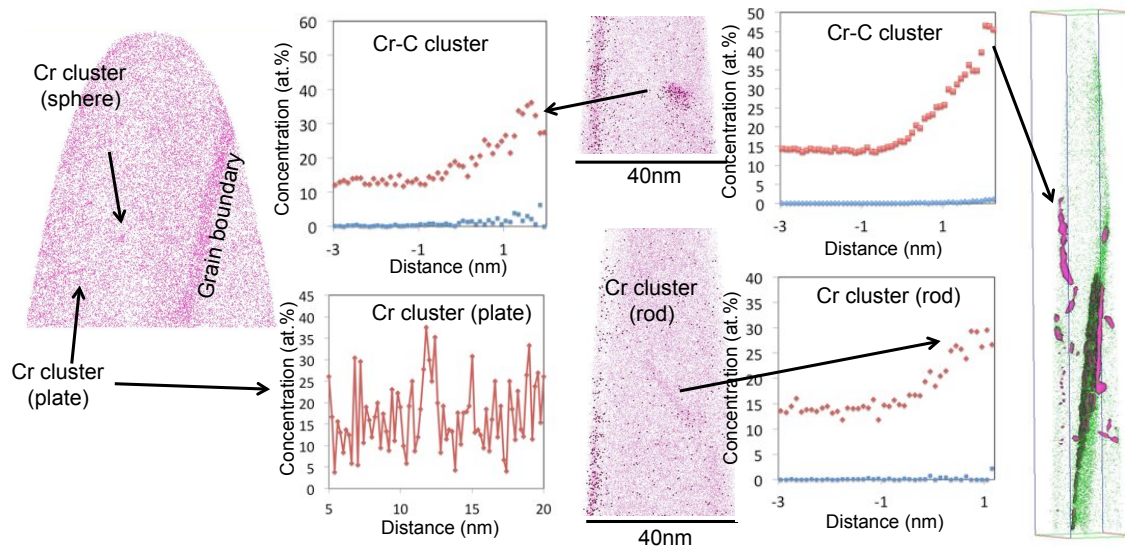
Figure 12: Fe-15 at.% Cr alloy irradiated at 500 $^{\circ}$C revealing different Cr segregation features.

6.2. Grain boundaries

The ion-irradiated data is more complicated to interpret, due to surface interactions, shallow irradiation depth, and apparent carbon contamination, as highlighted below.

6.2.1. Irradiation at 300 $^{\circ}$C

Fe-15Cr – 1 dpa: Three different analyses of the same boundary at three different depths within 0.5 um from the surface showed significant uniform Cr and C segregation (**figure 13**). The average composition of the "grain boundary phase" is 25.8 ±2.1 at.% Cr - 1.8±0.4 at.% C – 0.5 ±0.06 at.% N, where the variations are the standard deviations from the 3 measurements.

Fe-15Cr – 10 dpa - Two different grain boundaries were analyzed. One grain boundary is uniformly decorated with thin square plates of a Cr carbonitride phase with the measured composition of 62.5 at.% Cr -18.5 at.% Fe-13.5 at.% C-5.5 at.% N, which is consistent with a $M_{23}(C,N)_6$ phase (**figure 14**). The grain boundary region between the particles is depleted in Cr. Four different analyses performed within 0.8 um from the surface on this first boundary consistently show the same particles and composition.

The second boundary exhibits Cr segregation with lower Cr content than the saturated phase found at 1 dpa (**figure 15**). Again, the four different analyses performed within 1 um form the surface systematically show the same Cr segregation.
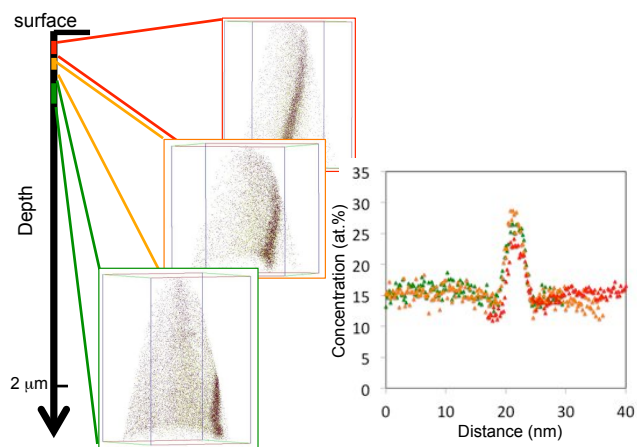
Figure 13: Grain boundary from the Fe-15 at.% Cr implanted at 300 ^{o}C – 1 dpa.
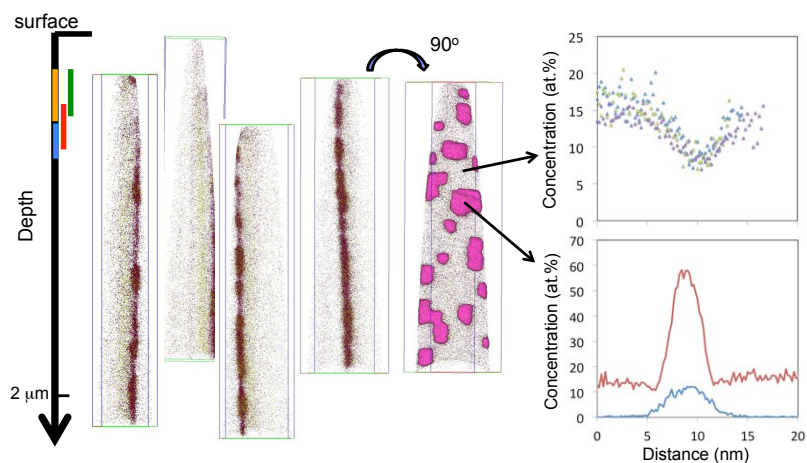
Figure 14: Grain boundary from the Fe-15 at.% Cr implanted at 300 ^{o}C – 10 dpa.
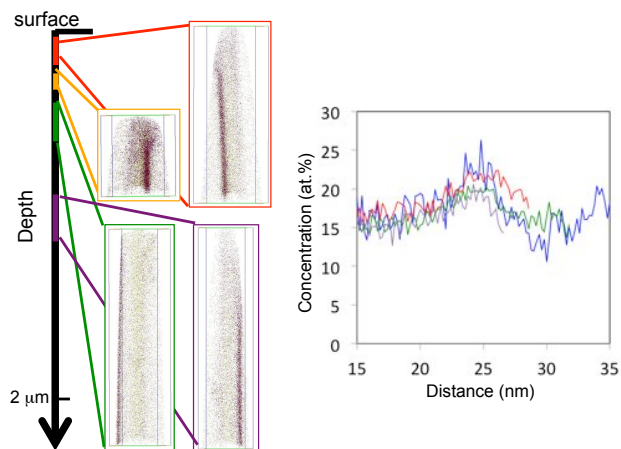
Figure 15: Grain boundary from the Fe-15 at.% Cr implanted at 300 ^{o}C – 10 dpa.

6.2.2. Irradiation at 500 ^{o}C – 1dpa

Fe-5Cr - The chemistry of a Σ17 grain boundary was analyzed through depth from the implanted surface to 2.25 um below surface. The reconstructions are shown in **Figure 16**. Nitride precipitates are observed both in the irradiated and non-irradiation regions, suggesting that they were either already present in the as-received alloy or formed thermally during irradiation. Profiles through the boundary were taken at different depths. Cr depletion is found in the dataset closest to the surface and in the data in the non-irradiated region. Alternatively, Cr segregation is observed further in depth. Notably, segregation is observed even close to a nitride precipitate (profile #2). The Gibbsian excess of Cr along the boundary varies from -4 atom/nm^2 to +3 atom/nm^2. The evolution of the grain boundary concentration with depth shown in **Figure 17** might suggest a strong effect of the surface with Cr depletion and irradiation induced segregation (0.6 - 1 um). However, the effect of grain boundary precipitation and associated sensitization may also play a role in the observed behavior.
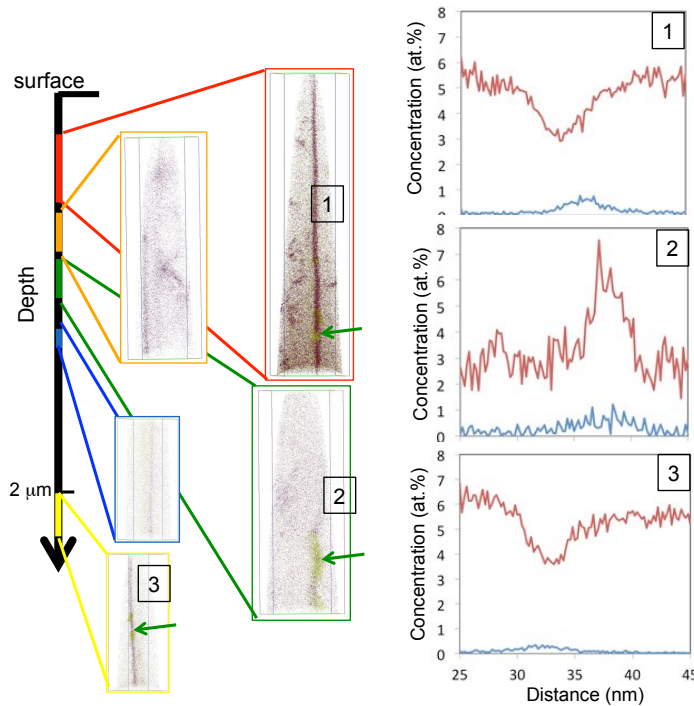
Figure 16: Analysis of a Σ17 grain boundary in Fe-5Cr at 500 ^{o}C – 1 dpa.
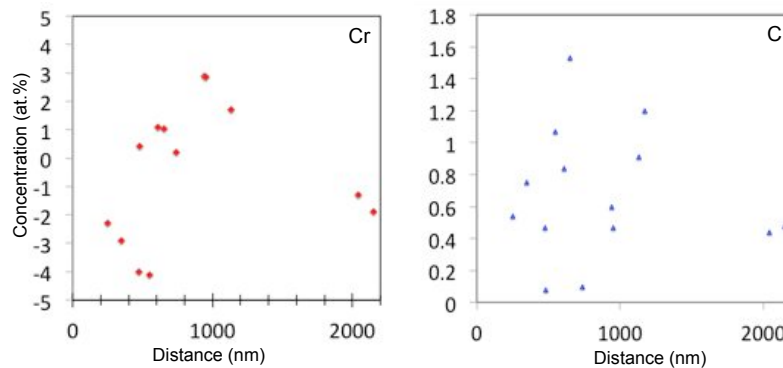
Figure 17: Gibbsian excess as a function of depth for the Σ17 grain boundary

Fe-15Cr – Two analyses were performed on the same boundary (**figure 18**). One analysis shows Cr depletion with a width of about 12 nm and the other reveals significant segregation with a peak at ~ 25 at.% Cr with a width of 6 nm.
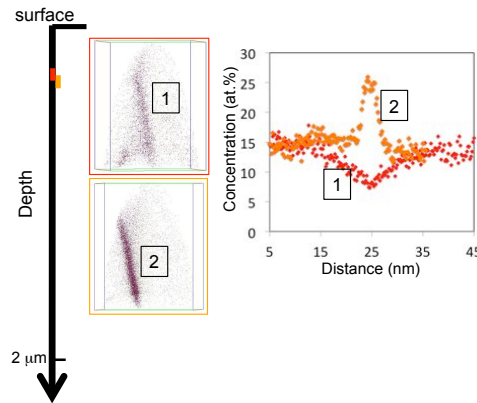
Figure 18: Grain boundary in Fe-15 at.% Cr at 500 ^{o}C – 1 dpa.

A grain boundary analyzed in a higher dose samples (10 dpa) also showed a variety of behaviors (**figure 19**): a slight depletion of Cr closest to the surface and in the irradiation region, the presence of higher Cr levels similar to the one reported in the 1 dpa condition with concentrations peaking a16 ~ 25 at.% Cr, and elsewhere a W shape profile with an overall depletion and local segregation at the boundary. The saturated behavior is found in thin plates which would suggest the presence of a "phase" with a measured composition is 28 at.%Cr – 2.8 at.%C – 0.5 at.%N.
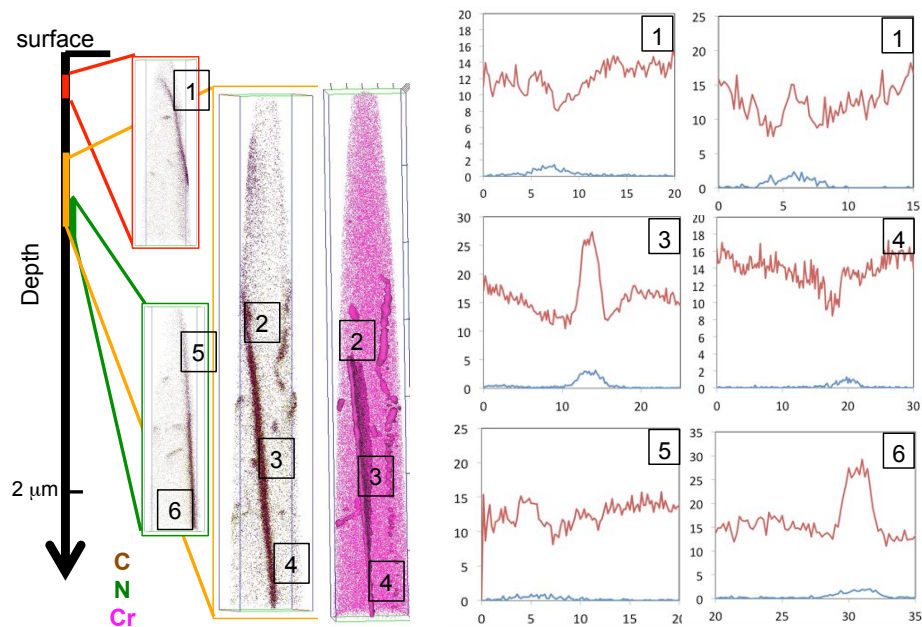
Figure 19: Chemistry as a function of depth for one grain boundary from the Fe-15 at.% Cr alloy at 500 ^{o}C – 10 dpa.

Finally, the measured C concentration in all boundaries are compiled in **Figure 20**. The results suggest significant contamination from the surface or by irradiation.
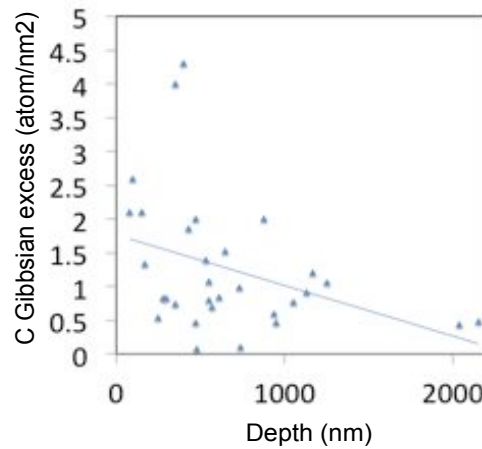
Figure 20: Carbon Gibbsian excess for all grain boundaries in all alloys and condition point measured

6.3. Low dose rate ion irradiation

An initial low dose rate ion irradiation was performed at Sandia National Laboratory in collaboration with Khalid Hattar to investigate possible dose rate effects. The Fe-15 at.% Cr alloy was implanted using 5 MeV Fe^{++} ions at 300 $^\circ$C at a dose rate of 10^{-5} dpa/s and maximum dose of 10 dpa. Analyses reveal Cr clustering. However the Cr content in the particles is lower than that of the expected α' phase with only 45 to 50 at.% Cr. The number density is also significantly lower than in the neutron-irradiated alloy. Further irradiations are being conducted to high doses and different temperatures to map the dependence of α' precipitation and quantify possible ballistic effects.
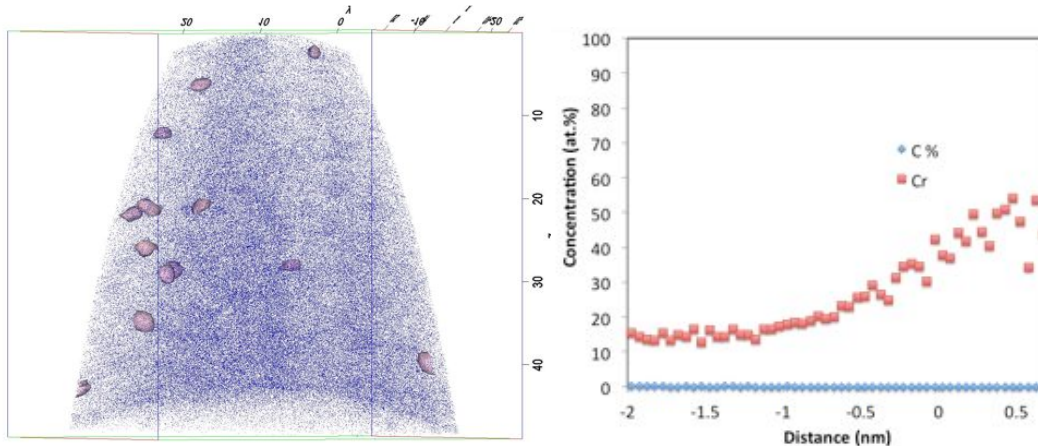
Figure 21. Low dose rate ion implanted Fe-15 at.% Cr alloy. Reconstruction and proxigram revealing Cr clustering with Cr composition between 45 and 50 at.% Cr.

7. Microstructure after neutron irradiation

7.1. Cr behavior in the matrix

Representative subsets (50 x 50 x 20 nm^3) taken from larger dataset are shown in **Figure 22** for each of the six alloys. The Fe-3 at.% Cr and Fe-6 at.% Cr alloys show uniform Cr distribution. The high Cr containing alloys exhibit Cr-rich clusters with increasing number density and decreasing cluster size with increasing Cr content.
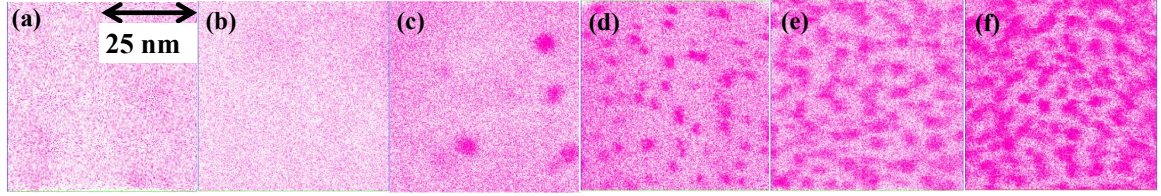
Figure 22. 20nm thick slices showing the distribution of Cr atoms for each of the analyzed alloys: (a) Fe-3Cr (b) Fe-6Cr (c) Fe-9Cr (d) Fe-12Cr (e) Fe-15Cr (f) Fe-18Cr.

A quantitative analysis of Cr clustering was performed based on the cluster finding algorithm described in [46-49]. The 'maximum separation distance', d_{max} defining whether Cr atoms are part of a same cluster, is chosen based on the comparison between the pair-distance distributions obtained from the measured data and randomized dataset as illustrated in **Figure 23** for a dataset from the Fe-18Cr alloy. The choice of d_{max} is important since too small a value can lead to clusters being artificially split into several clusters while a too large value can lead to clusters being merged into one. An additional parameter N_{min} sets the minimum number of atoms in statistically significant clusters to avoid counting small clusters that may occur in randomly distributed solutions. N_{min} is chosen based on the cluster size distribution in a randomized dataset. The frequency distribution of the number of Cr atoms in clusters shows two distinct groups of clusters. The small clusters correspond to truncated clusters present at the edges of the analyzed volumes and those are ignored in the present analysis. The d_{max} values are found between 0.4 and 0.6 nm, while the N_{min} values lie between 30 and 100. Finally, visual inspection of the filtered data is used to corroborate the choice for these parameters.

The observed atomic density inside the clusters is almost 2.4 times that of matrix, which is indicative of the well-known magnification effect [44, 50, 51] that operates in many alloy systems such as Fe-Cu for instance [52], where Cu, like Cr rich α', has a lower evaporation field than Fe [53]. The magnification effect implies a smearing of the cluster interface typically over 1-2 nm [44] with Fe ions originating from the matrix being projected into the clusters, therefore leading to measured cluster compositions with artificially high Fe content. To minimize the amount of extra Fe being included in the composition measurements, cluster compositions were determined from proximity histograms [54] allowing the selection of the position of the matrix/cluster interface and therefore minimize the overlap interfacial region. A high concentration value is chosen (2.5 to 3 times the measured Cr concentration in the matrix) to define the precipitate/matrix interface. The composition values reported in **Table 4** are averages over all clusters for a given alloy. Proximity histograms for the Fe-(9-18) at.% Cr alloys are shown in **Figure 23** confirming that the same phase forms for all alloys exhibiting Cr clustering with an average measured Cr concentration in the clusters of 86 at.% Cr. These Cr-rich clusters are consistent with the α' phase.
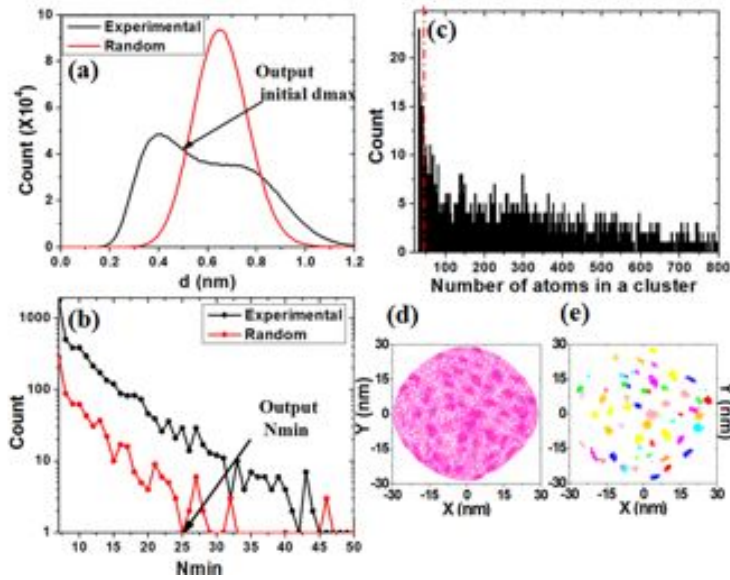
Figure 23. Determination of the parameters defining Cr clusters: (a) *dmax* selection, (b) *Nmin* selection (c) Frequency distribution highlighting truncated clusters, and (d) data filtering.

Table 4. Clusters and matrix characteristics measured for the neutron irradiated alloys containing 9 to 18 %Cr.

	No. density α'	Matrix (at.%)	Volume fraction	Radius (nm)
Fe-9 at.% Cr	(8.5 ± 0.1) X 10^{22}	8.9 ± 0.2	0.006	2.3
Fe-12 at.% Cr	(9.5 ± 0.2) X 10^{23}	9 ± 0.3	0.015	1.5
Fe-15 at.% Cr	(3.2 ± 0.3) X 10^{24}	9.7 ± 0.6	0.033	1.3
Fe-18 at.% Cr	(5.3 ± 0.5) X 10^{24}	10 ± 0.6	0.057	1.2
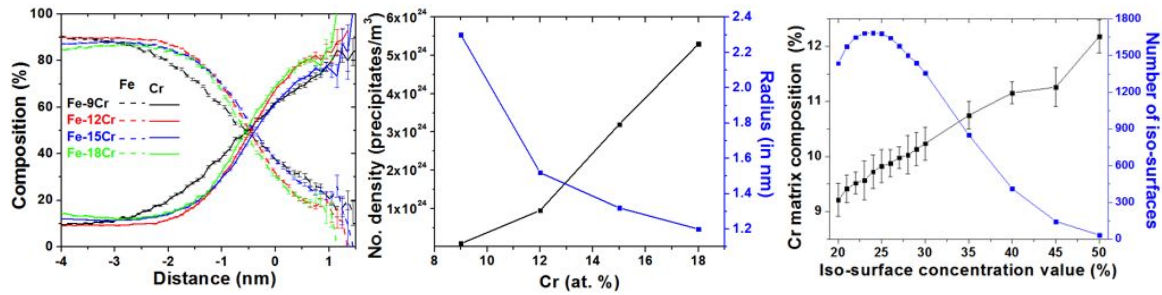
Figure 24. (a) proximity histogram (b) Precipitate radius and volume fraction for Fe-9 to18Cr alloys (c) Matrix composition determination by proxigram method demonstrated on Fe-15Cr.

The radius (R^{Cr}) of the Cr-rich clusters is calculated by using the spherical equivalent radius [55] given by:

$$R^{Cr} = \sqrt[3]{\frac{3N_{prec}}{4\pi\rho Q}}$$

where N_{prec} is the number of detected Cr atoms in each precipitate, ρ is the density of the precipitate (assumed to be identical to α-Fe, 84.3 atom/nm³), and Q is the detection efficiency of atom probe in use (taken to be 0.36). The average cluster sizes decrease with increasing Cr alloy concentration, as illustrated also in **Figure 23.** The number density (N_d^{Cr}) of Cr-rich precipitates is determined by:

$$N_d^{Cr} = \frac{N_p \rho Q}{N_{tot}}$$

where N_p is the number of measured precipitates in reconstructed volume. N_{tot} is the total number of atoms in the reconstructed volume. The number density for α′ precipitates for each Fe-Cr alloy is given in **Table 4**. The volume fraction (φ^{Cr}) is determined by:

$$\varphi^{Cr} = \frac{\Sigma N_{prec}}{N_{tot}}$$

where ΣN_{prec} is the sum of all Cr atoms contained in the Cr precipitates within the analyzed volume and N_{tot} is the total number of atoms in the reconstructed volume.

Matrix compositions were determined from proximity histograms. As shown in **Figure 24** for the Fe-15 at.% Cr alloy, the number of generated surfaces and the matrix composition both depend on the value of Cr concentration used to define the iso-concentration surface used as the matrix/precipitate interface. A maximum number of iso-surfaces shown insight in **Figure 24** is found for iso-concentration values between 23 and 25 at.% Cr. Higher values lead to small clusters being ignored and therefore high apparent matrix concentration while lower values leads to clusters being merged with matrix regions and therefore low apparent matrix compositions. Thus, the optimum iso-concentration value corresponding to the maximum number of detected clusters is chosen to report the matrix concentration values shown in **Table 4.**

7.2. Behavior of impurity elements

7.2.1. Distributions in the Fe – 6 at.% Cr alloy

After neutron irradiation, Cr and Si decorated dislocation loops and clusters are observed in the matrix as illustrated in **Figure 25**. The combined number density of loops and defect clusters is 2.9 ±0.7 x 10²² m⁻³. The observed spatial distribution of Cr- and Si-enriched dislocation loops suggest a defect-free region 20 to 25 nm wide on either side of grain boundaries. Two types of dislocation loops are observed based on the Si and Cr spatial distributions. The smaller loops exhibit Cr enrichment at their periphery with Si atoms located inside, as shown in **Figure 26**. For the larger loops, the spatial positions of Si and Cr atoms are the same, i.e. segregated on the outside of the dislocation line. The sizes of these visible dislocation loops are determined from the spatial distributions of Si and Cr. The size distribution shown in **Figure 26(e)** highlights the two populations of loops: smaller loops with diameters 8 to 10 nm and larger loops with diameters about 18 to 20 nm. Using the crystallographic orientation of the APT data reconstructions, the habit planes of the dislocations were indexed using the direction of the normal to the loop habit planes. These are distributed along a zone line between the <110> and <112> directions.
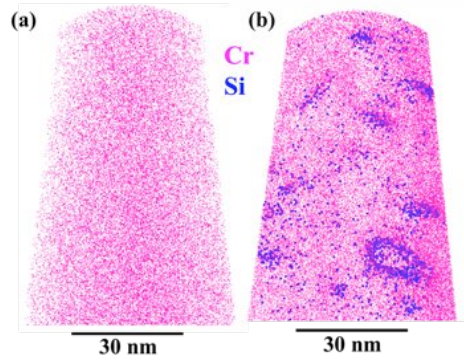
Figure 25: Representative 10nm thick slices from reconstructed datasets from (a) the as-received alloy and (b) the irradiated material.
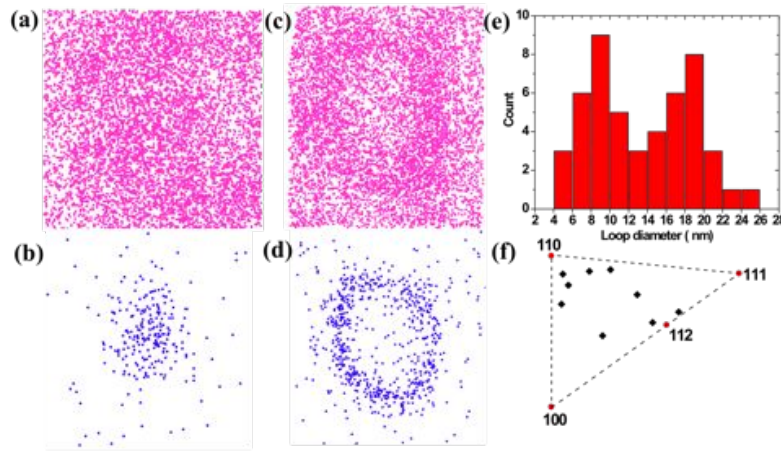
Figure 26: (a) Cr and (b) Si distributions with the same thin slice containing a small dislocation loop (c) Cr and (d) Si distributions with the same thin slice containing a larger dislocation loop (e) size distribution of the visible dislocation loops. (f) Distribution of the normal to the habit planes for visible dislocation loops.

7.2.2. Distribution in the Fe-15 at.% Cr alloy

Homogeneously distributed Si-P-Ni-Cr enriched clusters are also observed in the matrix after irradiation. An 0.8 at.% P threshold iso-concentration surface was used to define these clusters and estimate their compositions. A representative proximity histogram shown in **Figure 27** yields an average composition for the Si-P-Ni-Cr enriched clusters of 25.0±1.8 at.% Cr, 2.8±1.8 at.% Si, 1.2±0.4 at.% P, 4.7±0.7 at.% Ni. The mean radius and number density of these clusters is estimated to be 2±0.3 nm and (5.4±0.4) x10^{22} m^{-3}, respectively. The latter is almost two orders of magnitude lower than that of the α′ precipitates. Some of the α′ precipitates and Si, P, Ni, Cr clusters are joined, suggesting that one nucleated on the other.
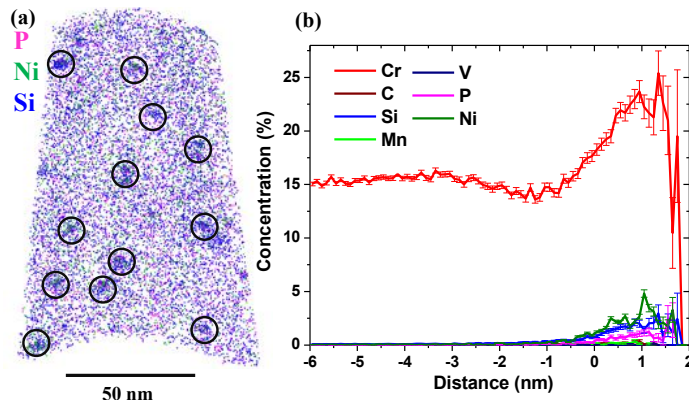
Figure 27. (a) 3D distribution of P, Ni, and Si atoms from the neutron irradiated condition. Encircled are clusters encriched in P, Si, and Ni. (b) Proxigram taken from clusters shown in (a). Insight is magnified part showing distribution of Si, P, and Ni and table showing content of clusters.
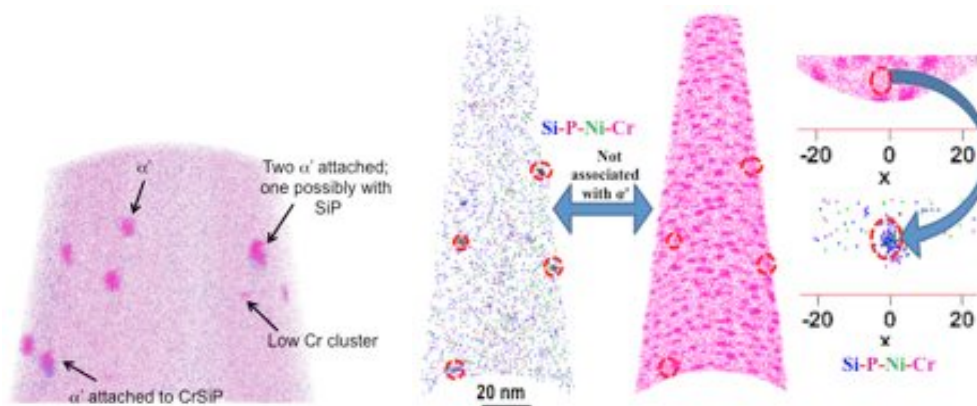
Figure 28: α' and SiPCrNi clusters in Fe-15 and 18 at.% Cr

7.3. Grain boundaries

The comparison between the Cr behavior for high angle random boundaries in the as-received and neutron-irradiated conditions is shown in **Figure 29**. Cr exhibits a flat concentration profile in the as-received Fe-6 at.% Cr alloy while it is segregated to the grain boundaries in the more concentrated alloys. After irradiation, all alloys exhibit Cr segregation with no significant changes for the alloys exhibiting α' precipitation (i.e. Cr > 9at.%).
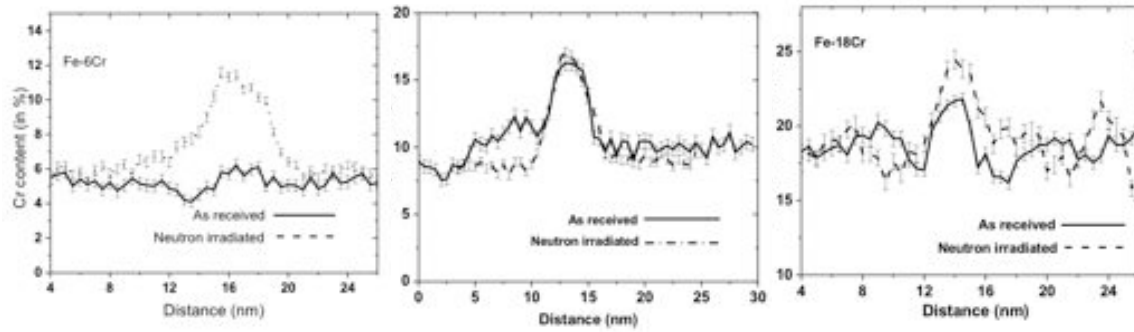
Figure 29: Grain boundary chemistry before and after neutron irradiation (left) Fe-6 at.% Cr, (middle) Fe-9 at.% Cr (right) Fe-18 at.% Cr.

Note that widths and heights of segregation profiles cannot provide quantitative measurements of segregation behavior due to inherent technique artefacts such as beam spreading in TEM [56] or trajectory aberrations in APT [57]. We are rather providing Gibbsian excess values in **Table 5**. For reference, the equivalent plane coverage or α' thickness along (100) planes using 85 at.% Cr for the α' phase composition is also calculated.

Table 5: Gibbsian excess (atom/nm^2) calculated using the matrix composition in case the alloy exhibits phase separation

Alloy	Fe-3 at.% Cr	Fe-6 at.% Cr	Fe-9 at.% Cr	Fe-12 at.% Cr	Fe-18 at.% Cr
Matrix	11.1	30	39.7	41.4	65
Equivalent α' thickness along (100) (nm)	0.15	0.42	0.55	0.58	0.9

7.3.1. Effect of grain boundary orientation studied in the Fe-6 at.% Cr alloy

In order to quantify the role of grain boundary misorientation, analyses were carried out on specific grain boundaries: a low angle boundary with a misorientation angle smaller than 14°, a $\Sigma 3$, a $\Sigma 5$, and a random grain boundary with a misorientation angle greater than 15°. The measured Gibbsian excess values [58] are 10.5, 7.6, 10.5, and 10.8 atoms/nm^2 for the low angle, the $\Sigma 3$, the $\Sigma 5$, and the large angle random boundary respectively.

Carbon is the main impurity element observed at a high angle boundary of the as-received alloy, while no significant phosphorus and little silicon are observed (**Figure 30**). Comparatively, segregation at a large angle grain boundary of the irradiated alloy is enhanced for Si and P but slightly less for C. The segregation levels observed in the irradiated alloy appear to depend on grain boundary orientation: no or little segregation is observed for C and P at the $\Sigma 3$ and low angle boundaries while clear segregation peaks are observed for the $\Sigma 5$ and large angle boundary (**Figure 31**).

One of the analyses from the low angle grain boundary showed the presence of Cr and Si segregated along line features that are interpreted as dislocation lines, as shown in **Figure 32**. From the measured distance between the dislocation line (d ~ 9 nm), the misorientation angle for the grain boundary is about 3° (using a value of the Burgers vector of 0.248 nm).
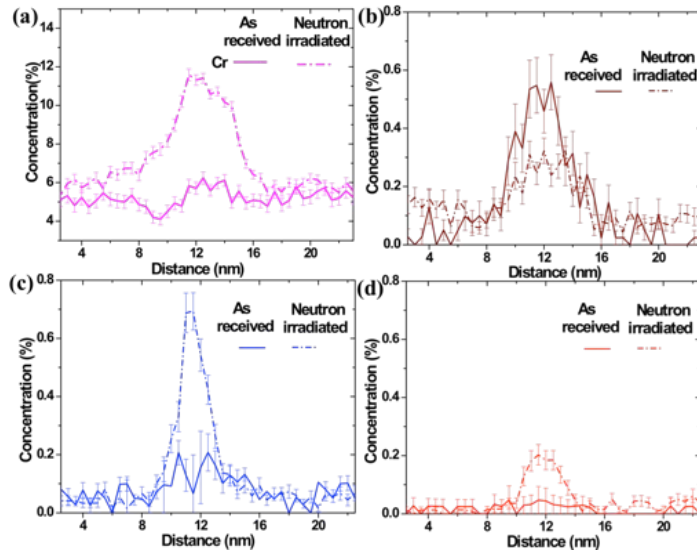
Figure 30: (a) Cr, (b) C, (c) Si, and (d) P concentration profiles before and after irradiation for random high angle grain boundaries
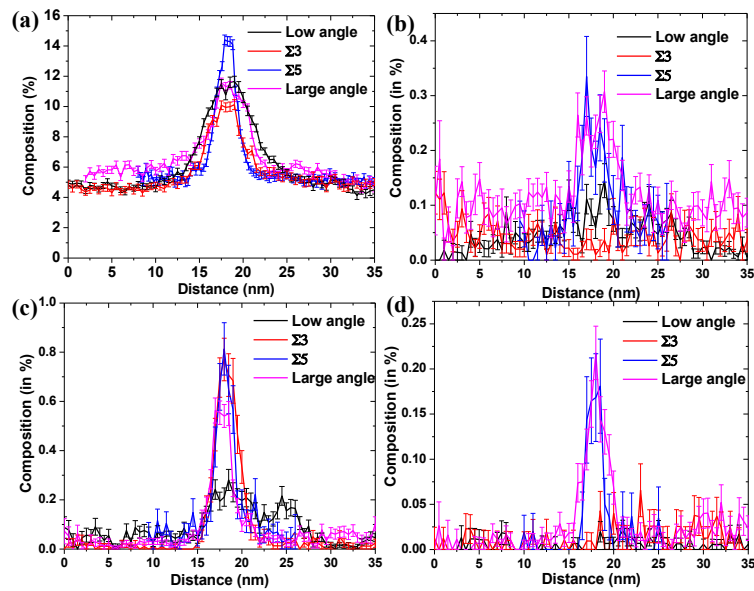
Figure 31: (a) Cr, (b) C, (c) Si, and (d) P concentration profiles across different types of grain boundaries after neutron irradiation.
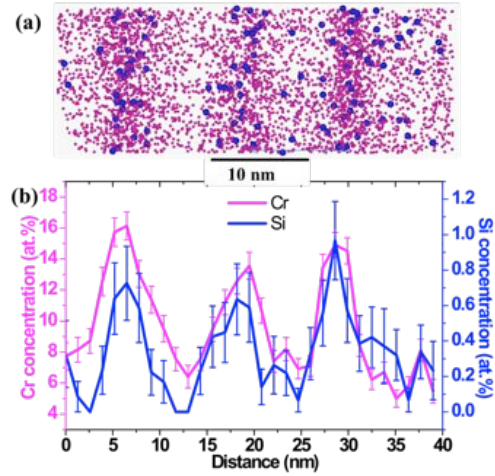
Figure 32: Cr and Si distribution with the low angle grain boundary plane

7.3.2. Effect of sensitization studied in the Fe-15 at.% Cr alloy

The grain boundaries in both the pre- and post- irradiation conditions are decorated by a high density of chromium nitride and chromium carbide particles. For reference, the Cr, Si, C, and P concentration profiles across a grain boundary with a misorientation angle greater than 15° in the as-received condition are shown in **Figure 32**. The particular profiles were taken within 20 nm of a carbide particle present at the boundary.
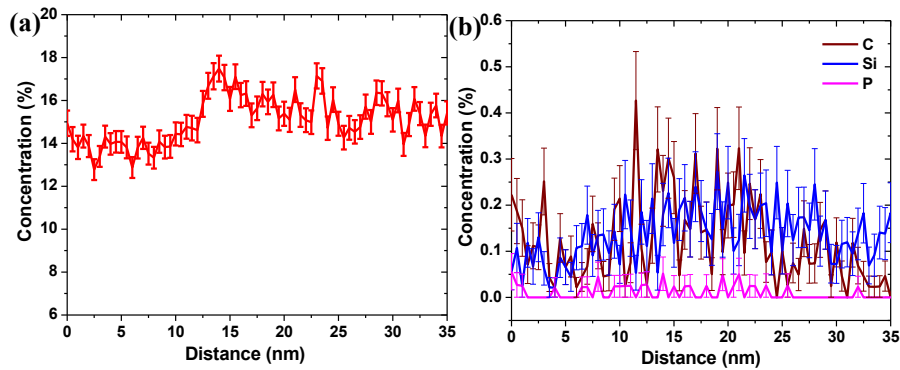
Figure 33: (a) Cr and (b) minority elements segregation profiles across a large angle random grain boundary in the as-received condition.

Two particular grain boundary orientations ($\sum 5$ and a $\sum 3$) were selected for analysis in the post-irradiation condition. The $\sum 5$ grain boundary had a very dense distribution of precipitates, and the Cr concentration profile taken next to a carbide particle exhibits a "W" shape, as shown in **Figure 33**.

Conversely, the $\sum 3$ grain boundary shows Cr segregation with an asymmetrical segregation profile across the grain boundary (**Figure 34**). The maximum to minimum Cr concentration ratio is highest for the $\sum 5$ boundary (with a W-profile) and lowest for the $\sum 3$ boundary; however these ratios are qualitatively similar. The behavior of Si, C, Ni, and P generally follow the Cr trends, i.e. W-shaped profiles at the $\sum 5$ grain boundary and asymmetric segregation profiles at the $\sum 3$ grain boundary. However, the distribution of some elements in the as-received condition also appears to be asymmetric.
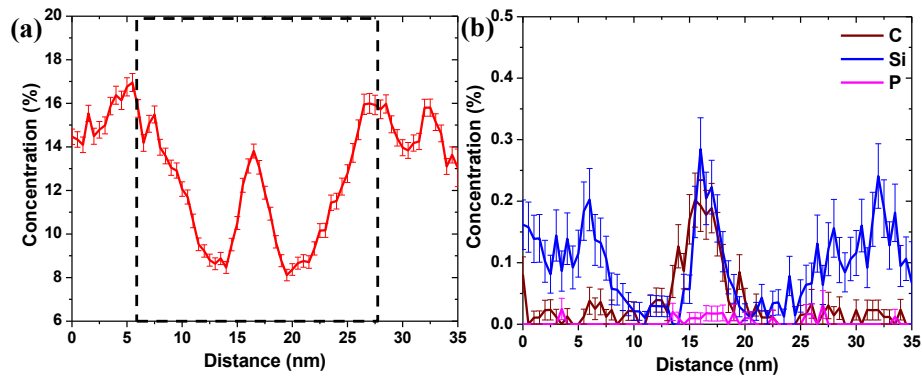
Figure 34. (a) Cr and (b) C, Si, and P segregation profiles across a $\sum 5$ grain boundary. The dashed line in (a) indicates the extent of the α' depleted zone.
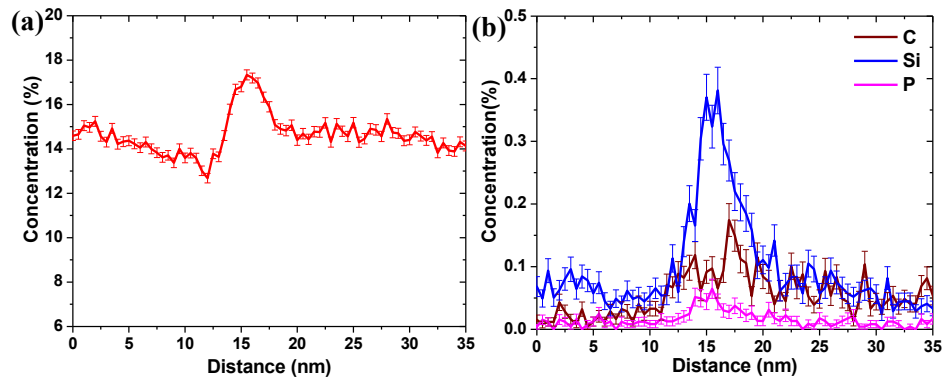
Figure 35. (a) Cr and (b) C, Si, and P segregation profiles across a $\sum 3$ grain boundary

Chromium carbide and nitride precipitates are present at the grain boundaries in both the as-received and neutron-irradiated conditions. The compositions of the precipitates are summarized in **Table 6**. All possible mass spectra peak overlaps were taken into account and deconvoluted. The distribution profiles across the carbide and nitride particle interfaces in **Figure 35** show comparable slight Cr depletion at the interphase boundaries. Following irradiation, the depletion is more pronounced with an average Cr concentration about 9 at.% Cr compared to 15% Cr in the adjoining regions and extends to a much larger width (~10-15 nm). The Cr depleted region around the particles is devoid of α' precipitates, as can be seen from 3-D reconstructed data in **Figure 36**. Si and P also segregate at the carbide and nitride interfaces (not shown), again with a 15-20 nm wide depletion zone away from the interfaces. Additionally, the Cr concentration in both precipitate types is slightly increased in the irradiated condition.

As a side note, **Figure 37** shows a comparison between the mass spectra from the carbide precipitate of irradiated (black colored) and as-received (red colored) sample. Boron (B) present in the carbide particle from a neutron irradiated sample is found to be mono-isotopic (^{11}B) whereas B from as-received condition is found in its natural isotopic distribution. The absence of ^{10}B in the irradiated condition is attributed to the transmutation reaction: ^{10}B + ^{1}n → ^{7}Li + ^{4}He. Since B is present in negligible quantity, it unlikely to create any substantial population of He bubbles.

Table 6: Chemical composition (in at. %) of carbide and nitride phases observed in as received and neutron irradiated samples measured with atom probe tomography.

		Cr	Fe	C		P, Si, Mn, V, Ni, B
Carbide	As-received	59.2± 2.0	21±1.5	19.5±1.2		<0.1
	Neutron irradiated	61.8± 2.2	11.9±1.1	26±1.5		<0.1
					N	P, Si, Mn, V, Ni, B
	As-received	68.6±2.5	2.7±0.5	6.4±1.1	22±1.4	<0.1
Nitride	Neutron irradiated	71.3±3.1	2.2±0.5	6±0.9	20±1.8	<0.1
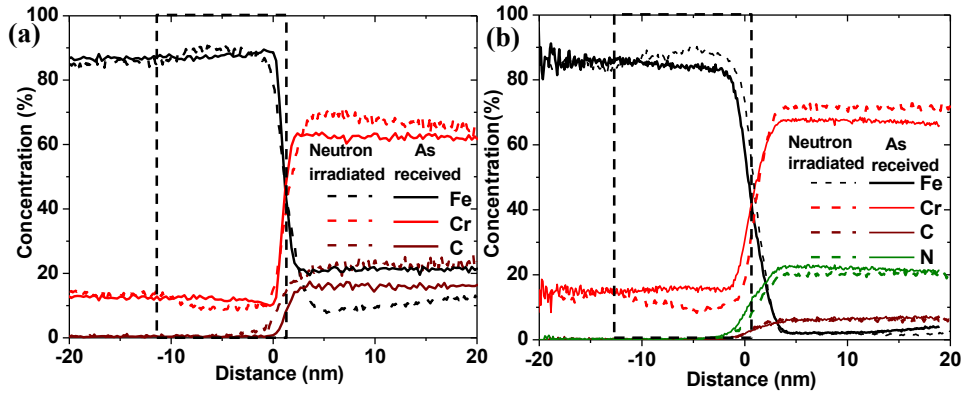
Figure 36. Distribution profiles taken across (a) carbide and (b) nitride interfaces in the neutron-irradiated Fe-15 at.%Cr alloy.
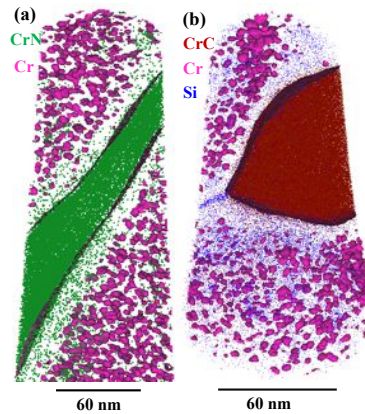
Figure 37. 3-D distribution of α' clusters (shown by iso-surfaces ≥ 34 at.% Cr) from the neutron-irradiated condition with (a) a nitride particle shown in green and (c) a carbide particle shown in brown.
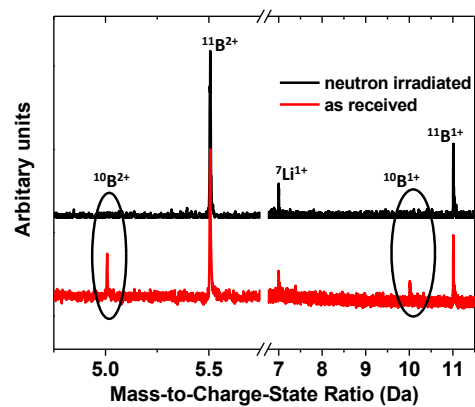
Figure 38. Partial mass spectra from carbide particles in the as-received and neutron-irradiated conditions.

8. Post neutron irradiation annealed Fe- 18 at.%Cr

8.1. Thermal stability of α' precipitates

Thermal annealing treatments were led and performed by Prof. Odette Group at UCSB. These experiments had several objectives including to selectively anneal defects (Si-P clusters, dislocation loops, α' precipitates) to determine their contribution to hardening and to test the thermal stability of the microstructures observed after irradiation.

At 500 °C, the α' precipitates coarsen, i.e. the average size increases, the number density decreases. We note that the matrix compositions changes, which is associated with the different temperatures used for the irradiation (300 and 500 °C respectively). The longer annealing at 500 °C yields a measure of the Cr solubility at this temperature: 13.2 at.% Cr. However, a similar conclusion may be reached from the alloys neutron-irradiated at 300 °C where the matrix composition is 8.9 at.% Cr and the observed microstructures may not be at thermal equilibrium.

At 600 °C, all precipitates dissolved indicating that the alloy is now in the α region. The increase in the measured α' concentration with annealing times is a reflection of the spatial limitation of atom probe tomography for small precipitates and perhaps a slight depletion of Cr in the α' precipitates formed during irradiation.
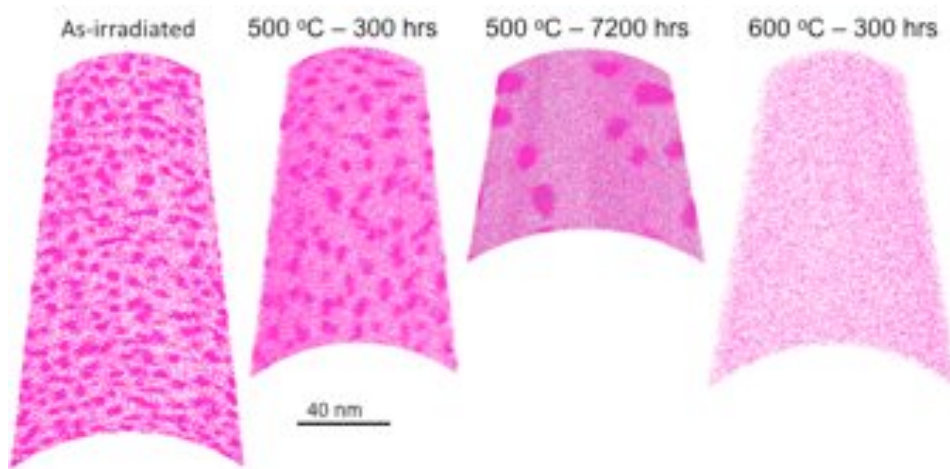
Figure 39: APT reconstructions comparing the microstructures observed in the Fe- 18 at.% Cr alloys after neutron irradiated and post irradiation annealing at 500 and 600 °C.

Table 7: Precipitate and matrix characteristics following post-irradiation annealing

	α' (at.%)	Matrix (at.%)	Number density (/m^3)	Radius (nm)
As-irradiated (300 °C)	77.4	10 ± 0.6	5.3 x 10^{24}	1.2
500 °C, 300 hrs	81.7	14.5 ± 0.5	2.0 x 10^{24}	1.6
500 °C, 7200 hrs	86.9	13.2 ± 0.5	0.16 x 10^{24}	3.6
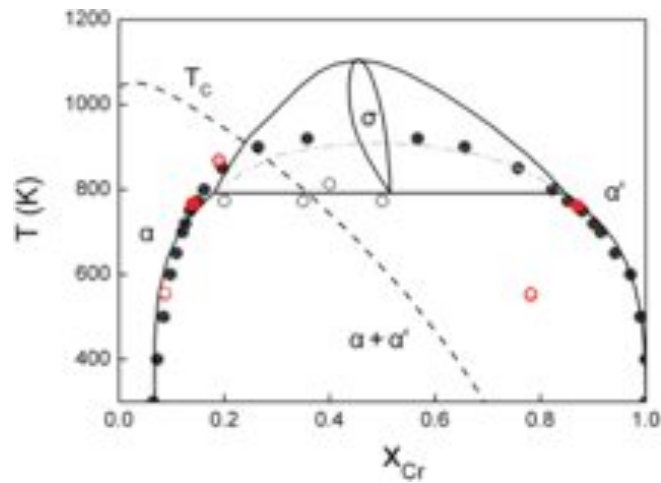
Figure 40: Compositional data compared to the Fe-Cr Calphad phase diagram and black dots from [59]. Note that the 300 °C may not correspond to thermal equilibrium values. The 600 °C composition is in the single phase region. The 500 °C α and α' phase compositions (filled circles) are in very good agreement with the phase diagram.
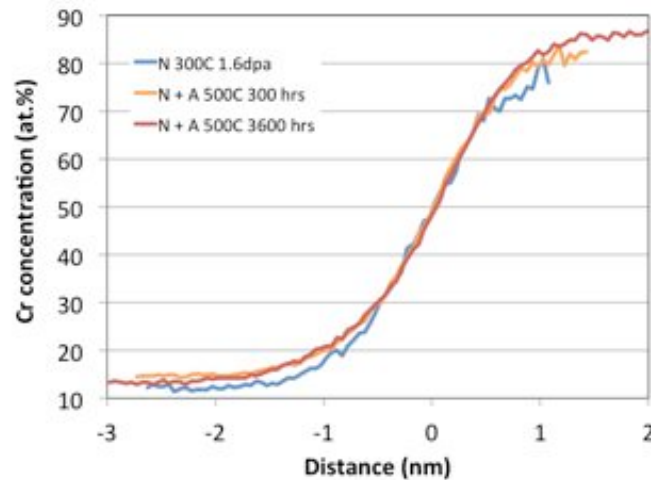
Figure 41: Proximity histogram on the α' precipitates using an isoconcentration surface of 50 at.% Cr and the smaller clusters were excluded except for the 7200 hours annealed samples for which all particles were included.

8.2. Grain boundary chemistry

Grain boundaries in the Fe-18 at.% Cr alloy were analyzed after the longer annealing at 500 °C. Segregation is Cr is observed with an α' depletion zone with a width of 50-100 nm. The measured Gibbsian excess is 24 atom/nm^2, not surprisingly smaller than the excess measure after irradiation at 300 °C. The baseline matrix has a higher Cr content at 500 °C and entropic effects should lead to a decrease in the segregation behavior with higher temperatures.
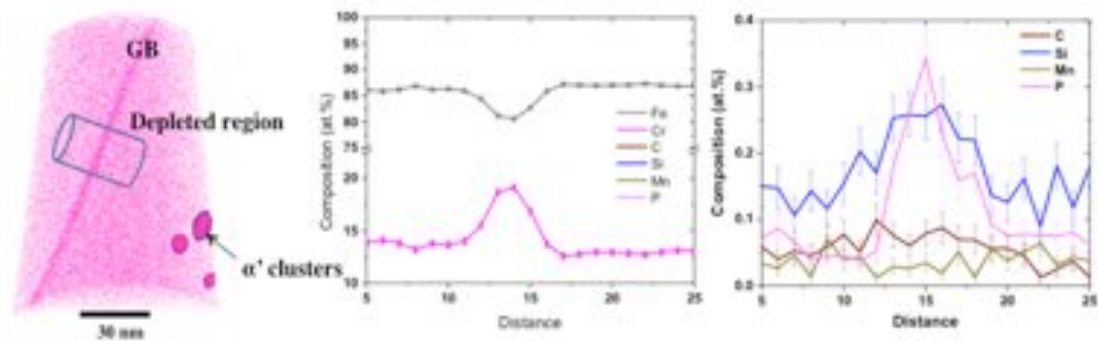
Figure 42: APT reconstruction from Fe-18 at.% Cr alloy after annealing at 500 $^{\circ}$C for 7200 hours – containing a grain boundary.
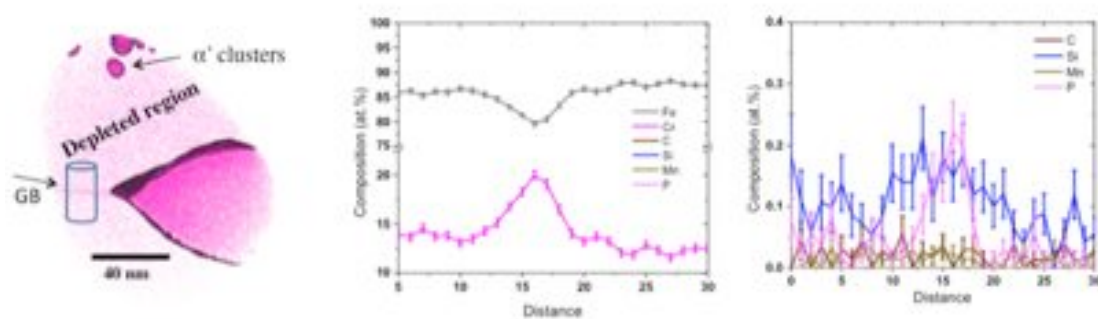
Figure 43: APT reconstruction from Fe-18at.% Cr alloy after annealing at 500 $^{\circ}$C for 7200 hours in the vicinity of a carbide particle

9. Modeling

Inverse Kirkendall Models of Radiation Induced Segregation in Cascade Damage Conditions

Aaron P. Selby[a,*], Aaron Kohnert[a], Benjamin Ramirez[a], Brian D. Wirth[a,b]

[a]*Department of Nuclear Engineering, University of Tennessee, Knoxville, TN 37996, USA*
[b]*Oak Ridge National Laboratory, P.O. Box 2008, MS6003, Oak Ridge, TN 37831, USA*

Abstract

This paper describes a modeling approach to simulate radiation induced segregation arising from the inverse Kirkendall effect in ferritic iron chrome alloys. The model considers only Frenkel pair damage initially, but is extended to examine cascade effects through the introduction of defect clusters with different properties than the monomer species. Both models were found to be extremely sensitive to the defect migration energies, as well as the fraction of defects produced in clusters. When these parameters are delicately chosen, some aspects of chromium segregation appear to follow experimental trends. Even in such cases, however, the dose dependence and bulk Cr concentration dependence were not accurately reproduced, suggesting that an inverse Kirkendall model may be too simple and too sensitive to the input parameters to accurately describe the mechanisms which drive segregation in irradiated engineering alloys, even when cascade effects are considered.

1. Introduction

Ferritic-martensitic (FM) steels and microstructural evolution and propety changes following high-energy particle irradiations are of considerable interest for Generation IV fission reactors and fusion reactors. Issues such as creep rupture strength, radiation hardening, phase stability and radiation induced segregation (RIS) are not fully understood for FM steels [1]. Of these issues, the understanding of RIS is of particular importance as it can lead to the formation of intermetallic phases, stress corrosion cracking, and other detrimental effects.

Predicting RIS in FM steels is complex due to the lack of consistent trends observed in experimental results. A literature review by Lu et al. reported on RIS in 15 different experiments in FM steels where 8 showed Cr enrichment and and 7 showed Cr depletion [2]. However, there were no systematic studies, making it difficult to draw any definite conclusions. More recently, a systematic study of 3 different alloys was performed by Was et al. by irradiating these alloys to doses from 1 to 10 dpa at 400°C and 500°C with 2.0 MeV protons at a rate of 1.3×10^{-5} dpa/s, finding that one alloy showed Cr enrichment, one showed Cr depletion, and yet another showed enrichment for one dose, and depletion for two other doses [3].

In other recent studies, Cr segregation has been observed to decrease with increasing temperature, as well as decreasing with increasing dose [4, 5]. Further, Marquis et al. concluded that

---

*Corresponding author
Email address:* `aselby1@vols.utk.edu` (Aaron P. Selby)

the Cr concentration was changing from a 'W-shaped' profile to a 'V-shaped' depletion profile with increasing dose [5]. Multiple studies have found Cr enrichment to decrease with increasing bulk Cr concentration [6, 7, 8].

The first modeling of RIS in dilute alloys was performed by Johnson and Lam in the late 1970s [9, 10]. The Johnson and Lam model included the effects of vacancy and interstitial diffusional encounters with solute atoms and diffusion of vacancy-solute and interstitial-solute complexes. RIS models for concentrated alloys are based on the relation derived by Manning[11]. Marwick developed a model utilizing the vacancy-solute coupling [12], and Wiedersich et al. went on to develop a model that incorporated solute coupling for both vacancies and interstitials [13].

Several rate theory models have appeared as well, including one developed to examine the impact of grain boundary structure on RIS behavior [14]. A recent Inverse Kirkendall (IK) model developed by Wharry et al. demonstrated an ability to reproduce many of the general trends in experimental data, but also displayed an intense sensitivity to several model parameters, particularly the defect migration energies [15].

To simulate RIS, we have implemented a spatially dependent, reaction-diffusion model using a formulation originally developed by Wiedersich et al. [13]. This paper seeks to investigate the sensitivity of the model through a systematic variation of material properties, as well as the dependence of Cr segregation on dose, temperature, and bulk Cr concentration. We have extended the model to include cascade effects.

2. RIS Model

This study uses a reaction-diffusion approach similar to the method developed by Wiedersich et al. [13]. This model accounts for the coupling of defect and atom fluxes through the use of preferential migration of interstitials and vacancies to Fe and Cr atoms in a binary Fe-Cr alloy. By defining the atom fluxes as occurring through vacancies and interstitials, the defect and atom fluxes are expressed in terms of concentration gradients and partial diffusivity coefficients of both the defects and the Fe and Cr atoms. We present two distinct models and analyze RIS behavior with both. The first considers only single vacancy and interstitial defects, similar to most prior rate theory models of segregation effects. The second considers clusters created by cascades via the introduction of additional equations. We refer to these as the Frenkel pair and cascade damage models respectively. For the Frenkel pair model, three coupled partial differential equations describe the one-dimensional (1-D) time and spatial dependence of the concentrations of interstitials, vacancies, and one of the alloying components under irradiation conditions.

2.1. General Rate Equations

The first two partial differential equations are the rates of change of the concentrations of interstitials (C_I) and vacancies (C_V) as a function of time and are described by the following equations:

$$\frac{\partial C_{\mathrm{I}}}{\partial t} = -\nabla \cdot J_{\mathrm{I}} + K_0 - R \tag{1}$$

$$\frac{\partial C_{\mathrm{V}}}{\partial t} = -\nabla \cdot J_{\mathrm{V}} + K_0 - R \tag{2}$$

2

The first terms on the right hand side (RHS) of equations (1) and (2), $\nabla \cdot J_\text{I}$ and $\nabla \cdot J_\text{V}$ are the divergence of the fluxes of interstitials and vacancies, respectively, and K_0 and R account for production from irradiation and recombination, respectively. The conservation equations for Fe and Cr are described by

$$\frac{\partial C_\text{Cr}}{\partial t} = -\nabla \cdot J_\text{Cr} \tag{3}$$

$$\frac{\partial C_\text{Fe}}{\partial t} = -\nabla \cdot J_\text{Fe} \tag{4}$$

where $\nabla \cdot J_\text{Cr}$ and $\nabla \cdot J_\text{Fe}$ are the divergence of the flux of Cr atoms and Fe atoms, respectively. However, equation (4) is not independent and may be omitted because $C_\text{Fe} = 1 - C_\text{Cr}$.

2.2. Diffusion Coefficients

Diffusion coefficients for both defects and alloying elements in the binary system are defined in terms of partial diffusivity, such that

$$D_\text{I} = d_\text{CrI}N_\text{Cr} + d_\text{FeI}N_\text{Fe} \tag{5}$$

$$D_\text{V} = d_\text{CrV}N_\text{Cr} + d_\text{FeV}N_\text{Fe} \tag{6}$$

$$D_\text{Cr} = d_\text{CrV}N_\text{V} + d_\text{CrI}N_\text{I} \tag{7}$$

where d_xy is the diffusivity of element x by exchange with defect y and N represents atomic fraction. Written in terms of the volumetric concentration using $N_i = \Omega C_i$, and eliminating Fe with $C_\text{Fe} = 1 - C_\text{Cr}$ gives

$$D_\text{I} = \Omega(d_\text{CrI} - d_\text{FeI})C_\text{Cr} + d_\text{FeI} \tag{8}$$

$$D_\text{V} = \Omega(d_\text{CrV} - d_\text{FeV})C_\text{Cr} + d_\text{FeV} \tag{9}$$

$$D_\text{Cr} = \Omega(d_\text{CrV}C_\text{V} + d_\text{CrI}C_\text{I}) \tag{10}$$

2.3. Flux Equations

The flux of interstitials produces a flux of Cr atoms and Fe atoms in the same direction of the interstitial flux. By contrast, the flux of vacancies drives a flux of Cr atoms and Fe atoms in the opposite direction of the vacancy flux. Accordingly, the defect fluxes are written

$$J_\text{I} = J_\text{Cr}^\text{I} + J_\text{Fe}^\text{I} \tag{11}$$

$$J_\text{V} = -(J_\text{Cr}^\text{V} + J_\text{Fe}^\text{V}) \tag{12}$$

where J_x^y is the flux of element x by exchange with defect y. These flux terms can be written as

$$J_\text{I} = -(d_\text{CrI} - d_\text{FeI})\alpha\Omega C_\text{I}\nabla C_\text{Cr} - D_\text{I}\nabla C_\text{I} \tag{13}$$

$$J_\text{V} = (d_\text{CrV} - d_\text{FeV})\alpha\Omega C_\text{V}\nabla C_\text{Cr} - D_\text{V}\nabla C_\text{V} \tag{14}$$

3

In equations (13) and (14), the first term on the RHS describes the Kirkendall effects for interstitials and vacancies, respectively, where the difference in constituent atom fluxes are made up by appropriate defect fluxes and α is a thermodynamics factor defined later.

The flux of Cr atoms is defined as

$$J_{\text{Cr}} = -D_{\text{Cr}}\alpha\nabla C_{\text{Cr}} + d_{\text{CrV}}\Omega C_{\text{Cr}}\nabla C_{\text{V}} - d_{\text{CrI}}\Omega C_{\text{Cr}}\nabla C_{\text{I}} \tag{15}$$

The first term on the RHS of equation (15) is the atom flux created by the concentration gradient. The second term and third terms on the RHS of (15) are the atom fluxes induced by the interstitial and vacancy gradients, respectively.

2.4. Thermodynamic Factor

The value of the thermodynamic factor, α, accounts for the difference between the chemical potential and the concentration gradient. Previous models used a value of 1 for this parameter, however, we have implemented a concentration-dependent value for α. To do this, the activity coefficients for the binary Fe-Cr system with atomic concentrations of Cr ranging of 0 at.% to 20 at.% at 700K were calculated using the Thermo-Calc software [16]. Using these activity coefficients along with the atomic fractions, the values of α were calculated as a function of Cr concentration. A curve was fit to this data, with the equation given as

$$\alpha = -2.1 \times 10^{-5}C_{\text{Cr}}^3 + 0.0013C_{\text{Cr}}^2 - 0.051C_{\text{Cr}} + 1 \tag{16}$$

for which the value of alpha decreases as the bulk Cr concentration increases. Our model uses equation (16) to calculate the value of α given the initial Cr concentration.

2.5. Extension of Model to Include Cascade Effects

As a first order approximation to introduce the basic physics of cascade damage, we considered two new defect types which represent interstitial clusters and vacancy clusters by introducing two additional equations into he model. We will refer to this extended model as the cascade effect model. The equations used to describe this model as written as

$$\frac{\partial C_{\text{I}}}{\partial t} = -\nabla \cdot J_{\text{I}} + \epsilon_{\text{I}}K_0 - R \tag{17}$$

$$\frac{\partial C_{\text{I,cluster}}}{\partial t} = -\nabla \cdot J_{\text{I,cluster}} + (1 - \epsilon_{\text{I}})K_0 - R \tag{18}$$

$$\frac{\partial C_{\text{V}}}{\partial t} = -\nabla \cdot J_{\text{V}} + \epsilon_{\text{V}}K_0 - R \tag{19}$$

$$\frac{\partial C_{\text{V,cluster}}}{\partial t} = -\nabla \cdot J_{\text{V,cluster}} + (1 - \epsilon_{\text{V}})K_0 - R \tag{20}$$

$$\frac{\partial C_{\text{Cr}}}{\partial t} = -\nabla \cdot J_{\text{Cr}} \tag{21}$$

The factors of ϵ_{I} and ϵ_{V} determine the production of interstitial and vacancy clusters, respectively. When both ϵ_{I} and ϵ_{V} are equal to one, no cascade effects are considered and only single interstitials and single vacancies are generated and the cascade model becomes equivalent to the

4

Table 1: Input Parameter Values

Definition	Symbol	Value	Unit	Reference
Fe Interstitial Formation Energy	E_{fI}^{Fe}	5.0	eV	[18]
Fe Vacancy Formation Energy	E_{fV}^{Fe}	1.6	eV	[19]
Fe Interstitial Migration Energy	E_{mI}^{Fe}	0.35	eV	[15]
Fe Vacancy Migration Energy	E_{mV}^{Fe}	0.625	eV	[15]
Fe Prefactor for Interstitial Diffusivity	$D_{0,I}^{Fe}$	6.59×10^{11}	$\frac{m^2}{s}$	[14]
Fe Prefactor for Vacancy Diffusivity	$D_{0,V}^{Fe}$	5.92×10^{12}	$\frac{m^2}{s}$	[14]
Cr Interstitial Migration Energy	E_{mI}^{Cr}	0.28	eV	[15]
Cr Vacancy Migration Energy	E_{mV}^{Cr}	0.55	eV	[15]
Cr Prefactor for Interstitial Diffusivity	$D_{0,I}^{Cr}$	6.85×10^{11}	$\frac{m^2}{s}$	[14]
Cr Prefactor for Vacancy Diffusivity	$D_{0,V}^{Cr}$	5.46×10^{12}	$\frac{m^2}{s}$	[14]
Vacancy Formation Enthalpy	S_{sv}	1.0	k_B	[20]

Frenkel pair model. The flux terms for the interstitial and vacancy clusters follow a similar form to the single interstitial and single vacancy flux terms. Initially, the concentrations of the defect clusters are set equal to zero, and the other initial conditions remain unchanged from the Frenkel pair model. Similarly, the boundary conditions remain the same, with the additional conditions of the two new defect cluster terms. We set the concentrations of the clustered defect terms equal to zero at the surface, and the gradients equal to zero at the foil center.

To solve this system of ODEs, we used the *ode15s* solver, a part of the ODE solver suite developed by MATLAB [17].

2.6. Parameters

The selection of accurate values for parameters is critical to obtain meaningful results from this model. The values for the parameters used in this model were chosen from published values taken from experiment and model calculations, and are shown in Table 1.

The values for the pre-exponential factor for interstitial or vacancy diffusion via Fe or Cr atoms come from Field et al. who used an Arrhenius fit to values calculated by Choudhury et al. from first principles [14, 21]. The vacancy formation energy value comes from a positron annihilation experiment in $\alpha - Fe$ [19]. The interstitial formation energy comes from ab initio calculations on defects in Fe-Cr systems [18]. The values for the migration energies were chosen for consistency with prior modeling work[15].

To simulate these new clustered defect terms, we introduced changes to the migration energies of the defect clusters. The migration energies of the Fe and Cr interstitial clusters were set equal to each other. This is because interstitial clusters are 1-d diffusers and are not expected to contribute to RIS. The migration energies of the Fe and Cr vacancy clusters were set higher that the single vacancies. This approximates to first order the dissociation barrier these clusters must overcome before diffusing and contributing to RIS. These values for cluster migration energies are shown in Table 2.

2.7. Initial Conditions

The initial concentrations of interstitials and vacancies are set to their thermal equilibrium values as shown in equations (22) and (23), and the concentration of Cr atoms is set uniformly across the spatial coordinate at the applicable volumetric concentration. Thus, the initial conditions are:

Table 2: Migration Energies for Interstitial and Vacancy Clusters

Definition	Symbol	Value	Unit
Fe Interstitial Cluster Migration Energy	E_{mI}^{Fe}	0.35	eV
Fe Vacancy Cluster Migration Energy	E_{mV}^{Fe}	1.225	eV
Cr Interstitial Cluster Migration Energy	E_{mI}^{Cr}	0.35	eV
Cr Vacancy Cluster Migration Energy	E_{mV}^{Cr}	1.15	eV

$$C_I(0, x) = \exp\left(-E_{IFe}^f/kT\right) \tag{22}$$

$$C_V(0, x) = \exp\left(-E_{VFe}^f/kT\right) exp\left(S_{sv}/k\right) \tag{23}$$

$$C_{Cr}(0, x) = C_{Cr}^0 \tag{24}$$

2.8. Boundary Conditions

At the foil center (x=L/2), symmetry boundary conditions are applied by setting the intersitial, vacancy, and Cr gradients equal to zero.

$$\frac{\partial C_I(t, \frac{L}{2})}{\partial x} = \frac{\partial C_V(t, \frac{L}{2})}{\partial x} = \frac{\partial C_{Cr}(t, \frac{L}{2})}{\partial x} = 0 \tag{25}$$

At the grain boundary (x=0), the interstitial and vacancy concentrations are set to their thermal equilibrium values. Further, the rate of change of the interstitials and vacancies at the grain boundary are set equal to zero, consistent with a black sink.

$$\frac{\partial C_I(t, 0)}{\partial t} = \frac{\partial C_V(t, 0)}{\partial t} = 0 \tag{26}$$

A Cr conservation condition replaces the boundary condition for Cr at the grain boundary by integrating over half the length of the spatial coordinate.

$$\int_0^{\frac{L}{2}} C_{Cr}(x, t) dx = C_{Cr}^0 \frac{L}{2} \tag{27}$$

where C_{Cr}^0 is the initial concentration of Cr atoms.

3. Results

3.1. Temperature Dependence

The Frenkel pair model with parameters as shown in Table 1 provided for enrichment across a wide range of temperatures and doses. To investigate the various dependences of the model, we used a default set of simulation parameters, as shown in Table 3.

Using the default simulation parameters and varying the temperature, we simulated the temperature dependence, as shown in Figure 1. The model was applied using two different boundary conditions. The first held defect concentrations at the grain boundary fixed at thermal equilibrium

Table 3: Default Simulation Parameters

Parameter	Value	Unit
Cr Concentration	9	at.%
Temperature	400	∘C
Dose	5	dpa
Dose Rate	1×10^{-5}	dpa/sec
Grain Thickness	2	μm

while the second assumed a black sink condition, where the interstitial and vacancy concentrations are set equal to zero at the boundary. In both cases, depletion of Cr is predicted at temperatures below about 250 K. As the temperature increases, the segregation behavior changes from depletion to enrichment, and the model matches the experimental results reasonably well. As the temperature increases above about 450°C, the behavior of the model results to diverge depending on the boundary conditions used. For the theral equilibrium boundary condition, the vacancy concentration near the grain boundary is locally dominated by thermal vacancies rather than irradiation induced vacancies. This enhances back diffusion of Cr and limits the amount of segregation that can occur. As such, the first term in Equation (15) balances the defect-flux induced flow of Cr toward the sink, the second two terms in Equation (15) [22]. Once again, this behavior is not present when a black sink is modeled, as the concentration of defects at the sink is zero.
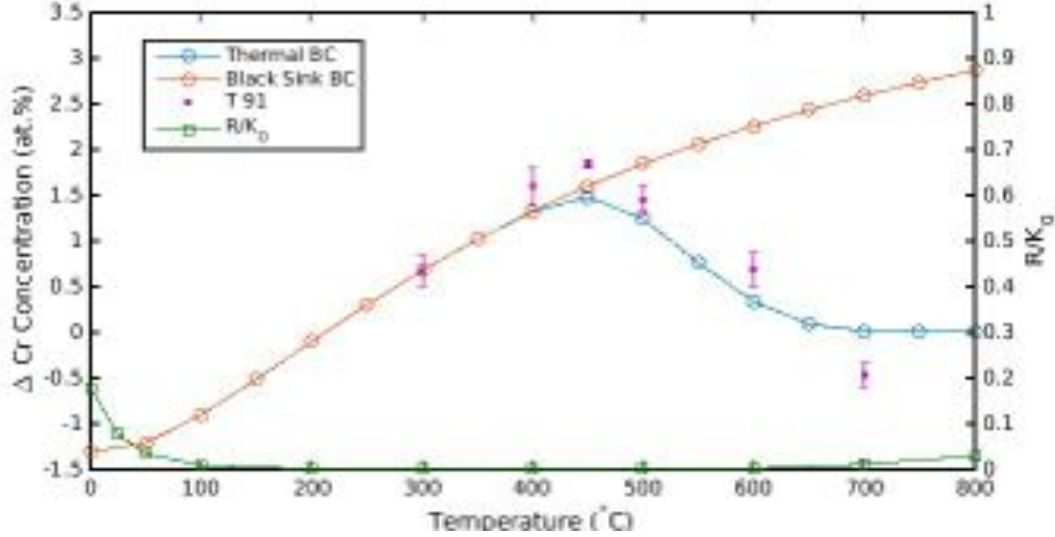
Figure 1: Final Cr concentration at the grain boundary and the ratio of the recombination rate to the production rate as a function of temperature. The experimental values come from the systematic study performed by Wharry et al. [8].

The effect of cascade damage on this temperature dependence was examined by varying the fraction of damage generated in clusters. Figure 2 shows the temperature dependence for several cases where the values of ϵ_I and ϵ_V are held equal, starting with all damage generated as monomers and increasing the clustered fraction 10 percent at a time. With only small fractions of the damage diverted to clusters, the enrichment seen in the Frenkel pair model immediately vansishes. The low

temeprature depletion seen in this parameter set occurs regardless of cascade effects, but with a slight increase in magnitude.
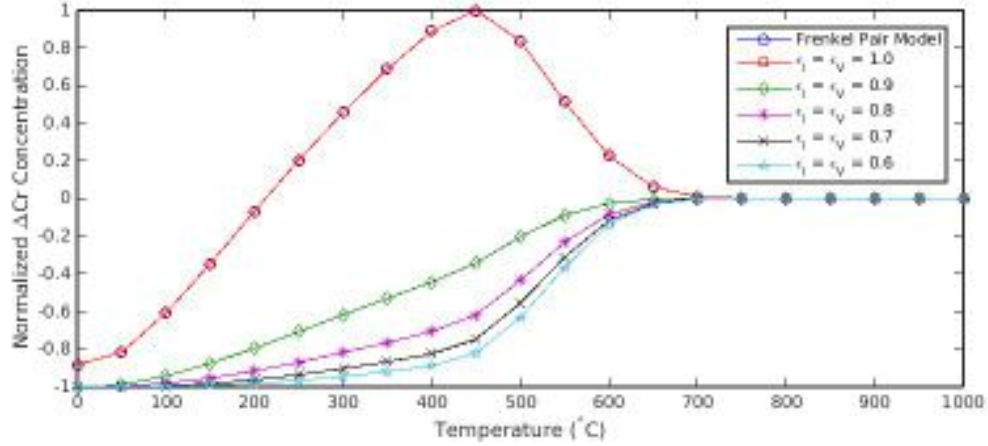
Figure 2: Comparing the final Cr concentration at the grain boundary as a function of the temperature as predicted by the Frenkel pair model and the Cascade model, using a thermal equilibrium boundary condition.

3.2. Sensitivity Analysis

[155]   Though resonable agreement with experimental data can be obtained from such a model it is clearly strongly impacted by cascade damage conditions, and correspondingly the agreement shown in Figure 1 may be fortuitous. There is one further reason to doubt the predictive capacity of these models as is, namely that the dependence of segregation on defect migration energies is extremely strong. To illustrate this point, we mapped the segregation behavior in a small phase space of
[160] migration energies for the Frenkel pair model using the default conditions in Table 3. The input parameter values were taken from Table 1, with the exception of the values of the migration energies in question. Figure 3 shows the results obtained from one of these simulations. Not only does the magnitude of segregation reach untenable values within changes of a few hundreds of an eV or less, but the nature of segregation can easily change from enrichment to depletion.
[165]   With changes in migration energies as small as 0.08 eV, Cr concentrations varied from almost complete depletion with 0.54 at.% Cr at the sink to near complete enrichment with 98.14 at.% Cr at the sink. Figure 3 shows how sensitive this model is to the values chosen for the migration energies. The range of experimental data spans enrichment and depletion values typically 5 % or less, which can easily be overwhelmed by a change in migration energies of less than 0.01 eV.
[170]   The sensitivity to migration energies is no less pronounced when cascade effects are included. This can be domonstrated following the same methods as in the sensitivity study for the Frenkel pair model, but with the fraction of unclustered damage ϵ_I and ϵ_V both set equal to 0.6. The input parameter values were held constant, with the exception of the values of the migration energies in question. Figure 4 shows the results obtained from these simulations. It is clear that the cascade
[175] model is still very sensitive to the values chosen for the migration energies, however the amount of segregation as determined from the migration energy gap has slightly shifted. Though enrichment does not occur in the cascade model using the default parameteriazation, it can be produced by

8
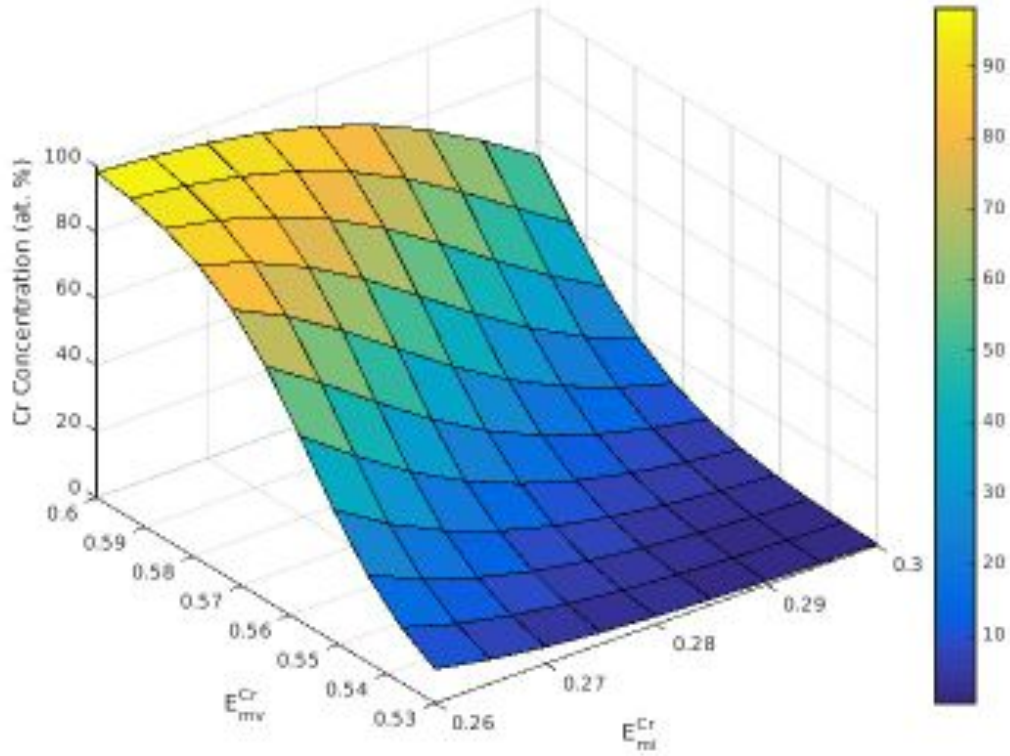
Figure 3: Final Cr concentration at the grain boundary as a function of the migration energy of interstitials and vacancies in Cr.

a small increase in the value of E_{mv}^{Cr} on the order of a few hundredths of an eV. Again, such an adjustment also substantially increases enrichment in the Frenkel pair model, and both models are strongly sensitive to the migration energies.

We explored the phase space of ϵ_I and ϵ_V in a similar manner to obtain a more detailed understanding of how these factors impact segregation. Figure 5 shows the final concentration at the boundary with the production bias factors varied fully from 0 to 1. These simulations use the default parameters listed in Table 3 with the exception of E_{mv}^{Cr}, which was set to 0.573 eV. The fraction of damage in interstitial clusters strongly impacts segregatation, with steadily decreasing enrichment as the unclustered fraction decreases. The fraction of vacancy clusters, on the other hand, does not seem to matter at all until nearly all of the damage is in vacancy clusters. This finding is intuitive in the sense that the clustered interstitials are removed as an enrichment driver, while vacancies are not. The slower kinetics associated with the vacancy clusters does not change their depletion prefence, and the same steady state condition is acheived in the long term regardless of how they are produced.

9
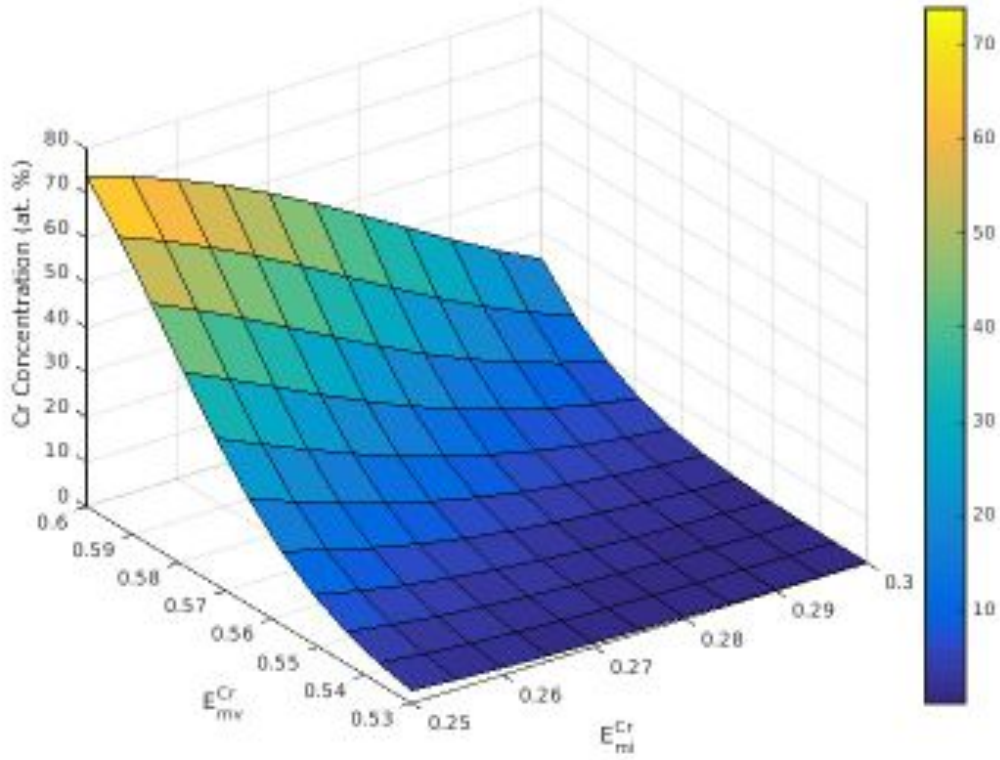
Figure 4: Final Cr concentration at the grain boundary as a function of the migration energy of interstitials and vacancies in Cr as predicted by the cascade model.

3.3. Dose and Dose Rate

The dose dependence for the Frenkel pair model is shown in Figure 6. The saturation of Cr enrichment is due to reaching a steady-state compositional gradient, and the back diffusion of Cr down this gradient, in which the first term in Equation (15) balances the defect-flux induced flow of Cr toward the sink, the second two terms in Equation (15) [22]. We also investigated the dose dependence of the cascade model with $\epsilon_I = \epsilon_V = 0.6$, and found little difference from the dose dependence of the Frenkel Pair Model. As before, the value of E_{mv}^{Cr} had to be increased to 0.573 eV to ensure enrichment behavior occured in the cascade model.

Investigating dose rate dependence on the segregation of Cr, we used default simulation parameters in the Frenkel pair model and varyied the dose rate as shown in Figure 7. At low doses, the interstitial and vacancy concentration introduced through irradiation are not high enough to overcome the concentrations from thermal equilibrium. Thus, the back diffusion of Cr dominates and there is very little Cr segregation. The role of thermal vacancy back diffusion is illustrated by comparison to a model where a black sink is assumed at the grain boundary instead of thermal equilibrium. As the dose rate increases, the concentrations of defects introduced from irradiation

10
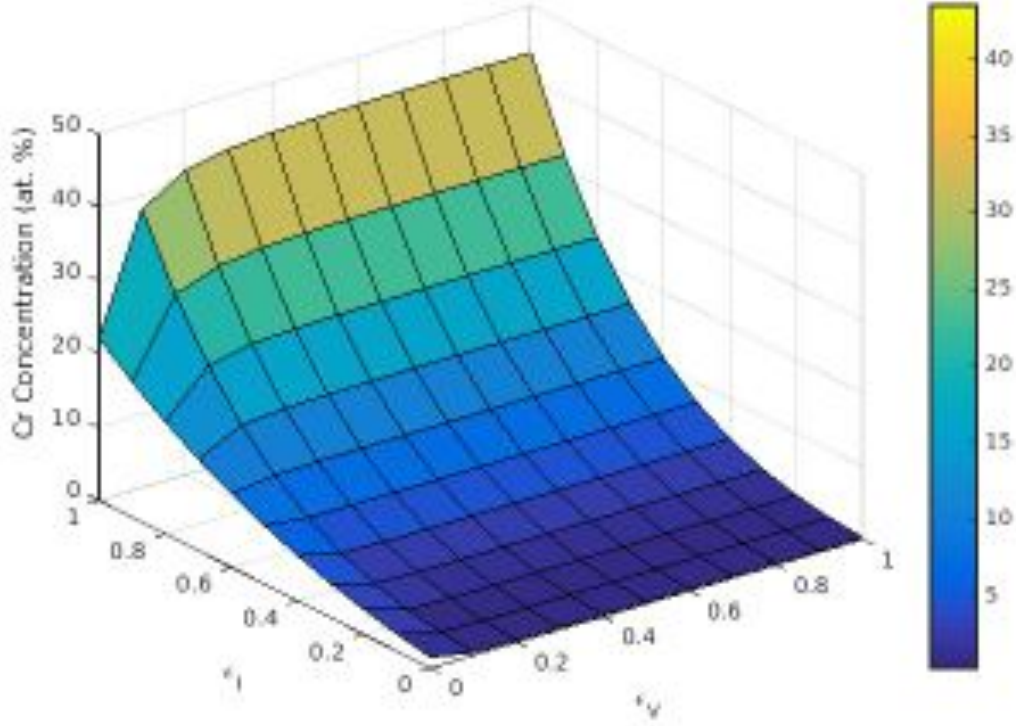
Figure 5: Final Cr concentration at the grain boundary as a function of the fractions of unclustered damage as predicted by the cascade model.

becomes greater than those from thermal equilibrium, and the Cr segregation increases. At the highest dose rates examined, the segregation begins to slightly decline. This is a result of an increasing proportion of defects annihilating through recombination, which is negligible at lower dose rates.

A series of simulations were performed to better understand the dependence of Cr enrichment on bulk Cr concentration. In these simulations, we used the same default simulation parameters and varied the Cr concentration. We found that the amount of Cr enrichment increased with increasing bulk Cr concentration. The reason for the increasing segregation with increasing bulk Cr concentration is due to the segregation terms in the model scaling with Cr concentration, and the back diffusion terms scaling with the Cr gradient. Therefore a high bulk concentration requires a sharper peak at the boundary to achieve balance. The opposite trend has generally been observed in experiments. The concentration dependent thermodynamic factor was not enough to account for the experimentally observed behavior.

11
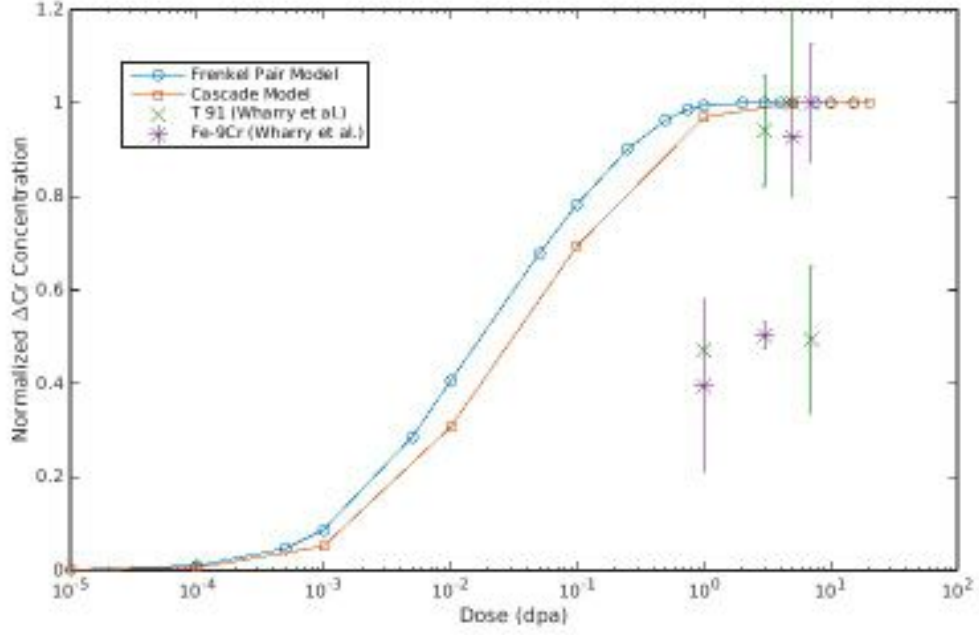
Figure 6: Excess Cr concentration at the grain boundary as a function of the dose as predicted by the Frenkel pair model and the Cascade model normalized to the saturation value. The experimental values come from the systematic study performed by Wharry et al. [8].

220 **4. Discussion**

4.1. Qualitative Analysis

When looking at the flux equations, some qualitative results can be inferred following Wiedersich et al. [13]. First, assuming steady state, the flux of Cr and Fe atoms must be equal to zero.

$$J_{\text{Cr}} = J_{\text{Fe}} = 0 \tag{28}$$

Further, because the effect of bias effects are neglected, the flux of interstitials must be equal to 225 the flux of vacancies. This must be true because equal numbers of interstitials and vacancies are generated by irradiation and equal numbers are lost by recombination. Thus, for steady state to be achieved, the flux of interstitials and vacancies to sinks must be equal.

$$J_{\text{I}} = J_{\text{V}} \tag{29}$$

∇C_{I} can be eliminated from (15) and a relationship between ∇C_{Cr} and ∇C_{V} can be derived.

$$\nabla C_{\text{Cr}} = \frac{\Omega C_{\text{Cr}} C_{\text{Fe}} d_{\text{CrI}} d_{\text{FeI}}}{\alpha(d_{\text{CrI}} C_{\text{Cr}} D_{Fe} + d_{\text{FeI}} C_{\text{Fe}} D_{Cr})} \times \left(\frac{d_{\text{CrV}}}{d_{\text{FeV}}} - \frac{d_{\text{CrI}}}{d_{\text{FeI}}} \right) \nabla C_{\text{V}} \tag{30}$$

12
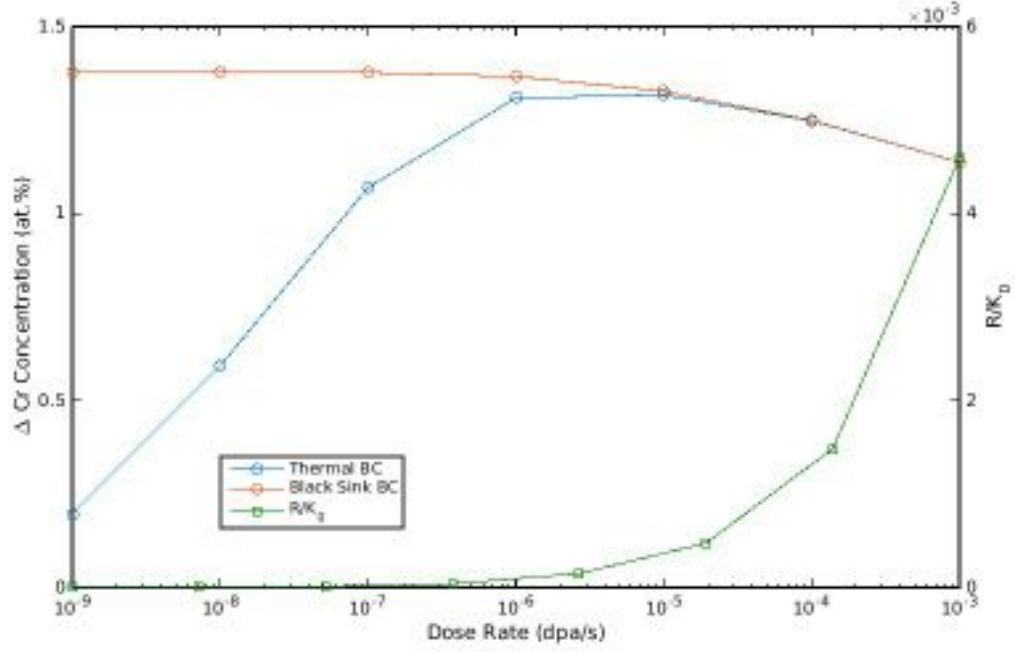
Figure 7: Change in Cr concentration at the grain boundary and the ratio of the recombination rate to the production rate as a function of dose rate.

The direction of the gradient of Cr atoms and vacancies is determined from the term in parentheses on the right of the multiplication sign in equation (30),

$$\nabla C_{\mathrm{Cr}} \propto \frac{d_{\mathrm{CrV}}}{d_{\mathrm{FeV}}} - \frac{d_{\mathrm{CrI}}}{d_{\mathrm{FeI}}} \tag{31}$$

It is clear that the relative ratios of the diffusivities determine the sign of equation (31), and this relationship has long been used as a qualitative explaination for why enrichment or depletion occurs. During irradiation, the concentration of vacancies always decreases toward the sink, e.g. $\nabla C_{\mathrm{V}} > 0$. If $d_{\mathrm{CrV}}/d_{\mathrm{FeV}} > d_{\mathrm{CrI}}/d_{\mathrm{FeI}}$, equation (30) will be positive and the concentration of Cr will also decrease toward the sink. This leads to a depletion of Cr at the surface. Conversely, if $d_{\mathrm{CrV}}/d_{\mathrm{FeV}} < d_{\mathrm{CrI}}/d_{\mathrm{FeI}}$, equation (30) will be negative and the gradient of Cr will be opposite that of the vacancy gradient, leading to an enrichment of Cr at the surface.

This equation explains the temperature dependence of our results. At low temperatures, the ratio of the vacancy diffusivity of Cr to Fe is higher than that of the interstitial diffusivity ratio, therefore the vacancy diffusion dominates driving Cr depletion. The ratio of the interstitial diffusion of Cr to Fe is greater at higher temperatures, and interstitial diffusion dominates, leading to Cr enrichment. For the parameters in this study, the temperature where the segregation of Cr crosses over from depletion to enrichment is predicted to occur around 200°C, and this is consistent with the plot of the temperature dependence.

13

The same analysis can be used to understand why these models are so sensitive to the defect migration energies. Upon closer examination,

$$\nabla C_{\mathrm{Cr}} \propto \frac{D_{0,\mathrm{V}}^{\mathrm{Cr}}}{D_{0,\mathrm{V}}^{\mathrm{Fe}}} \exp\left(\frac{E_{\mathrm{mV}}^{\mathrm{Fe}} - E_{\mathrm{mV}}^{\mathrm{Cr}}}{k_B T}\right) - \frac{D_{0,\mathrm{I}}^{\mathrm{Cr}}}{D_{0,\mathrm{I}}^{\mathrm{Fe}}} \exp\left(\frac{E_{\mathrm{mI}}^{\mathrm{Fe}} - E_{\mathrm{mI}}^{\mathrm{Cr}}}{k_B T}\right). \tag{32}$$

By writing the relationship in this way, it becomes apparent that the real driving force behind the magnitude of this value is the difference between the migration energies for the vacancy and interstitial diffusion mechanism, respectively. These "migration energy gaps" become the effective activation energies for RIS in this model. The difference in migration energy for exchage with different elements is on the order of a tenth of an eV or less. For this reason, small changes in any component migration energy can cause significant disruption in the migration energy gaps, drasticfally altering the magnitude or even direction of RIS. From equation (32), it is obvious that the sensitivity to migration energies is inherent to these models, and cannot be avoided. An important conclusions is that the uncertainty in such parameters well exceeds the order of precision required to make meaningful predictions from these models. Even should these properties be known to great precision, such strong sensitivities suggest that the effects of solute clustering, precipitation processes, impurity dragging, strain field interactions, and other effects that might be negligible or separable in other rate theory problems could strongly couple to the RIS problem and alter the behavior of the system entirely. Indeed, there has been some suggestion that concentration dependent migration energies may be necessary to capture aspects of RIS behavior[15].

Rather than stabilizing the system as the authors had hoped, the inclusion of cascade effects only added additional sensitivity and complication. The primary consequence of defect clustering (at least in bcc alloys) is to prohibit some fraction of the interstitial damage from contributing to segregation due the confined nature of the one dimensional diffusion tracjectories of interstitial clusters. Intuition suggests, and this study shows, that as the fraction of these clusters increases the interstitial driven segregation process becomes weaker. Thus, the authors suggest that if there is indeed an interstitial driven enrichment in these alloys, it would be weaker from proton irradiation than electrons, and weaker still from heavy ion or neutron damage. The volatile nature of these models, particularly with respect to migration energy prevents the authors form making concrete predictions or correlations with experimental results. Additionally, no consideration was made in this model for self clustering, which may become significant in certain temperature regimes and for large grains. Though these condsiderations add some uncertainty, a weaker interstitial segregation mechanism with dense cascades may play some role in making sense of the somewhat scattered data existing for RIS in these metals.

Though invaluable in qualitative analysis, the inverse Kirkendall mechanism alone clearly cannot act as a predictive model of RIS behavior. Certain aspects of the model, such as the magnitudes of segregation and temperature dependences can be easily manipulated through minute changes in parameter values, and fits to a desired trend are easily reverse engineered. Other aspects are quite characteristic of the model, and do not exhibit any parameter dependence at all. Unfortunately, many of these appear to fit empirical data for these alloys rather poorly. The dose dependence is an excellent example, where the early onset and saturation of RIS at doses below 1 dpa stand in stark contraditction to the existing data. Another is the dependence on bulk concentration, which is a fundamental consequence of the model as posed. A concentration dependent thermodynamic factor α does not disrupt this behavior, which also contradicts experiment. All of this suggests interactions and balances with other microstructural processes will be necessary to build a predictive model.

5. Conclusion

We applied the RIS modeling framework developed by Wiedersich [13] to the problem of chromium segregation in FM steels, and extended this framework to include the effects of cascade damage. Within some regimes, these models can be calibrated to give reasonable values given the chosen input parameters. For example, at intermediate temperatures, the model appears to compare well to experimental measurements. The temperature dependence of the model compared reasonably well with experiments, with a peak segregation occuring at about 450 °C, and a lack of segregation at higher temperatures due to the balancing of the back diffusion and defect flux terms. However, by performing a sensitivity analysis it became apparent that the model is extremely sensitive to the input parameters, particularly the values chosen for the migration energies. By perturbing the migration energies by as little as a few hundredths of an eV, the enriched Cr concentration at the sink could vary by more than 90 at.%. This extreme sensitivity was apparent in models with and without cascade damage.

The performance of this modeling approach suggests that the inverse Kirkendall mechanism, while a strong driving force for RIS, does not act alone and cannot be used in isolation as a fully predictive model of every aspect of segregation. The strong sensitivity of the magnitude, sense, and temperature dependence on migration barriers implies strong coupling to other microstructural processes through subtle impacts on these barriers. Additionally, the production of defect clusters in cascades decreased the effectiveness of the interstitial driven segregation mechanism. In this case, Frenkel pair damage caused significantly more enrichment than cascade damage.

References

[1] K. Murty, I. Charit, Journal of Nuclear Materials 383 (2008) 189–195.

[2] Z. Lu, R. Faulkner, G. Was, B. Wirth, Scripta Materialia 58 (2008) 878–881.

[3] G. S. Was, J. P. Wharry, B. Frisbie, B. D. Wirth, D. Morgan, J. D. Tucker, T. R. Allen, Journal of Nuclear Materials 411 (2011) 41–50.

[4] J. P. Wharry, Z. Jiao, V. Shankar, J. T. Busby, G. S. Was, Journal of Nuclear Materials 417 (2011) 140–144.

[5] E. A. Marquis, R. Hu, T. Rousseau, Journal of Nuclear Materials 413 (2011) 1–4.

[6] M. Bachhav, L. Yao, G. R. Odette, E. A. Marquis, Journal of Nuclear Materials 453 (2014) 334–339.

[7] M. Bachhav, G. R. Odette, E. A. Marquis, Journal of Nuclear Materials 454 (2014) 381–386.

[8] J. P. Wharry, G. S. Was, Journal of Nuclear Materials 442 (2013) 7–16.

[9] R. A. Johnson, N. Q. Lam, Physical Review B 13 (1976) 4364–4375.

15

[10] R. A. Johnson, N. Q. Lam, Journal of Nuclear Materials 69–70 (1978) 424–433.

[11] J. R. Manning, Physical Review B 4 (1971) 1111–1121.

325 [12] A. Marwick, Journal of Physics F: Metal Physics 8 (1978) 1849.

[13] H. Wiedersich, P. Okamoto, N. Lam, Journal of Nuclear Materials 83 (1979) 98–108.

[14] K. G. Field, L. M. Barnard, C. M. Parish, J. T. Busby, D. Morgan, T. R. Allen, Journal of Nuclear Materials 435 (2013) 172–180.

[15] J. P. Wharry, G. S. Was, Acta Materialia 65 (2014) 42–55.

330 [16] J. Andersson, T. Helander, L. Höglund, P. Shi, B. Sundman, Calphad 26 (2002) 273–312.

[17] MATLAB, version 8.4.0 (R2014b), Natick, Massachusetts, 2014.

[18] P. Olsson, C. Domain, J. Wallenius, Phys. Rev. B 75 (2007) 014110.

[19] H.-E. Schaefer, K. Maier, M. Weller, D. Herlach, A. Seeger, J. Diehl, Scripta Metallurgica 11 (1977) 803–809.

335 [20] T. Allen, G. Was, Acta Materialia 46 (1998) 3679–3691.

[21] S. Choudhury, L. Barnard, J. Tucker, T. Allen, B. Wirth, M. Asta, D. Morgan, Journal of Nuclear Materials 411 (2011) 1–14.

[22] P. Okamoto, L. Rehn, Journal of Nuclear Materials 83 (1979) 2–23.

16

10.   Discussion

10.1.   Alpha' precipitation

10.1.1. Neutron irradiation

The clear appearance of α' precipitates for alloys containing at least 9 at.% Cr suggests that the solubility limit for Cr at 290 °C is between 6 and 9 at.%. The observed formation of α' precipitates in these neutron irradiated Fe-Cr alloys may be the result of two competing phenomena: (1) an irradiation-accelerated mechanism where the point defect supersaturation allows the achievement of equilibrium at much faster rates than under thermal conditions, and (2) an irradiation-induced mechanism, where the coupling between migrating point defects and solute atoms (Cr) can induces a non-equilibrium state, and therefore can modify the composition range of the expected phases. However the clusters do not appear to be associated with a segregation site and ballistic mixing is likely not important at neutron irradiation damage rates. Thus if one assumes that the Fe-9 at.%. Cr alloy has reached equilibrium, the measured matrix composition would suggest a solubility limit of 8.9 at.% Cr (8.3 wt.% Cr) at the nominal 563 K. The increasing measured matrix concentrations with alloy Cr concentration already indicates that the slightly (10% at 18Cr versus 8.9% at 9Cr) may mean that these alloys are not fully decomposed and characterization of microstructures at a higher dose condition would be useful to further clarify this issue.

The solubility limit measured in the Fe-9Cr alloy is within the concentration range given by [16] and in excellent agreement with the published DFT calculations [60]. The results of this study are compared with the estimated phase diagram taken from the compilation published by Bonny et al. [60]. The α-α' phase separation starts just below 9 at.% Cr which is in agreement with the location of the miscibility gap suggested both from theoretical work simulating thermal annealing and from experimental work focusing on irradiated alloys [60].

The α' phase is observed to form finely dispersed precipitates in bulk and does not appear to be associated with radiation defects such as loops, which is consistent with a radiation-accelerated diffusion mechanism. The number density of clusters significantly increases with alloy Cr concentration while cluster sizes decrease. This dependence can be rationalized in terms of increasing driving force for α' nucleation as the Cr concentration in the alloy increases. Previous work on irradiated Fe-Cr alloys found α' precipitates in 12 %Cr and % alloys irradiated to 24.5 dpa at 400 °C. The precipitates were much larger in size (10-15nm) consistent with lower nucleation rate and possibly coarsening at higher temperatures [20]. More recent work on neutron irradiated Fe-Cr alloys at 300 °C up to 0.6 dpa also showed presence of nanometer scale α' precipitates for alloys with 9 and 12 %Cr [61]. TEM observations of irradiated Fe-9 %Cr at 370 °C and 403 °C did not report the presence of α' precipitates, suggesting that at these higher temperatures the alloy is within the solubility limit [62]. Radii and volume fractions of the α' precipitates for the 9 and 12 Cr alloys are also in agreement with previous SANS data from Mathon et al. [17] who focused on more complex alloys with Cr concentrations between 9 and 12 %Cr. They also reported a Cr solubility limit at slightly higher temperature (325 °C) of 7.2 at.% Cr in FM steels neutron irradiated to 2.9 dpa. However these steels contained significant amounts of other elements potentially changing point defect interactions and solubility limits.

Novy et al. investigating Fe-20%Cr alloys reported 83 at.% Cr at 500 °C for the α' composition [63], claiming little if no effect from trajectory aberrations. While the measured compositions are in agreement with this value, we would argue that the reported numbers is artificially low. The observed atomic density increase inside the clusters (2.4 times that of the matrix) strongly suggests a magnification effect. Future work will focus on quantifying this effect and correcting the measured concentrations. In the extreme case where α' precipitates would be pure Cr, the extra Fe ions to be

accounted for in the matrix would induce a negligible change for the matrix composition measured in the 9Cr alloy.

In summary, using a set of model alloys, the present work confirms the solubility limit previously predicted, strongly suggesting irradiation-accelerated precipitation of the α′ phase. The deviations from the conventional Fe-Cr phase diagram may be of crucial importance to provide explanations for the variation in the microstructure evolution and change of mechanical properties of Fe-Cr alloys and high-Cr steels under long-term annealing or neutron exposure.

10.1.2. Ion irradiation

Irrespective of the Cr content and irradiation temperature, no α′ was observed after ion irradiation, which is in agreement with prior observations.

The different behaviors between the Fe-5 at.% Cr and Fe-15 at.% Cr alloys at both 300 and 500 oC is striking. The more dilute alloy exhibits clear Cr clustering on dislocation loop planes while the more concentrated alloy shows significantly smaller Cr clusters and multiple Cr cluster morphologies. These differences may be due to the effects of Cr concentration on the nature and size of defects forming upon irradiation. Bhattacharya [25] found Cr enrichment within <100> dislocation loop planes in Fe-11 at.% Cr at 500 ^{o}C to 45 dpa with segregation of Cr up to 25 to 30 at.% Cr, which is consistent with our results. Several TEM studies on ion implanted Fe-Cr alloys at 500 ^{o}C have found that the nature of the loops is mainly of <100> type with spatial alignment along 100 directions in both Fe and Fe-Cr alloys [25, 64]. Jenkins [64] reported that the size of the loops change from a few hundreds nm in pure Fe to 10-20 nm in Fe-8Cr, suggesting that Cr changes number density and size which might explain the spatial distribution differences that we observed in the Fe-5 at.% Cr and Fe-15 at.% Cr alloys.

It is striking that all the Cr clusters observed here have similar Cr compositions around 30 at.% in both what might be considered an under-saturated alloy (Fe-5 at.% Cr) and an over saturated alloy (Fe-15 at.% Cr). The presence in both type of alloys would suggest that these clusters are not embryos of the α′ phase formed by competition between ballistic dissolution and thermodynamic phase separation but rather radiation-induced features.

10.1.3. Dose rate effects

The initial low dose rate ion irradiation suggests that a' may form through a spinodal like decomposition with increasing concentration with dose. Additional experiments at high dose will confirm whether the observed composition (45-50 at.%) and low number density reflect a transient state or a steady-state configuration reflecting of the combination of dose rate and temperature.

10.1. Radiation Induced segregation of Cr and other impurities

The evolution of microstructures under neutron irradiation is a result of competing mechanisms driven by thermodynamics and kinetics as modified by the high concentration of excess point defects generated by displacement damage (dpa). Atomic displacements form self-interstitial and vacancy defects, which can recombine, cluster in the form of extended defects like dislocation loops and nanovoids, or annihilate at defect sinks such as pre-existing dislocations, grain boundaries and other interfaces. The higher concentrations of mobile point defects, compared to normal thermal conditions, lead to radiation-enhanced diffusion (RED) and phase equilibrium at much shorter times than those normally expected at low temperatures. In addition to radiation enhanced precipitation (REP), preferential interactions of the migrating defects with alloying elements and impurities can lead to non-equilibrium microstructures, such as radiation induced segregation (RIS) to point defect sinks and radiation induced precipitation (RIP). Ideally the comparison between thermally treated and irradiated samples would clarify the controlling mechanism. In the case of the Fe-Cr system, however, the very slow kinetics of Cr diffusion under thermal conditions complicates the direct comparison.

10.1.1. Neutron irradiation

Grain boundary and Cr

The observations of Cr segregation in the neutron-irradiated alloys are consistent with either, or both, RED and RIS mechanisms. A RIS mechanism would imply a preferential Cr diffusion by interstitials and/or binding to vacancies in order to lead to the observed Cr segregation to grain boundaries during irradiation. However, accelerated diffusion kinetics under irradiation can also lead to Cr segregation at grain boundaries as would be expected under thermal conditions at longer times [65] and, therefore, a RED mechanism cannot be excluded. Indeed, the previously reported segregation enthalpy (-2895 J/mol [66]) would predict segregation levels that are comparable to those measured here. Assuming a RIS mechanism, the slightly lower Gibbsian excess of the Σ3 grain boundary of the Fe-5at.%Cr alloy can be explain by its smaller free volume and therefore lower sink strength, as previously reported for austenitic steels [67]. On the other hand, in the case of an accelerated kinetics RED mechanism, the lesser segregation at the Σ3 boundary may be consistent with its inherent lower interfacial energy and, especially, the Cr segregation enthalpy.

Analysis of grain boundaries in the Fe-15 at.% Cr alloy does not provide more clues. Similar levels of enrichment occur with and without irradiation. In addition, the presence of carbides is known to affect grain boundary chemistry independently of irradiation. The Cr peaks in the as-received condition clearly show that segregation takes place thermally, during the processing time-temperature history. Enrichment of Cr at grain boundaries has been observed in austenitic stainless steels [68] and ferritic steels [69]. The Cr enrichment is presumably controlled by the temperature dependent combination of the segregation energy mediated thermodynamic partitioning to the boundary, and diffusion rates. This is qualitatively consistent with a ratio of 1.25 shown in **Figure 27**. Non-equilibrium thermal segregation (TNES) may occur as well, leading to Cr enrichment at grain boundaries due to the flow and annihilation of excess annealing temperature thermal vacancies [70, 71]. Balogh reported a Cr grain boundary thermal segregation energy of 2900 J/mole, which produces a McLean model peak Cr enrichment ratio of $\approx$ 1.2 at the heat treatment temperature of 750°C [65]. Additional segregation could occur during cooling. As noted above, TNES could also result in GB enrichment in the as-received condition. In any event, some Cr boundary segregation is to be expected [35] in levels that are consistent with those observed.

We noted that thermal segregation is not unexpected, and that the magnitude of Cr enrichment levels is qualitatively similar between the as-received and neutron-irradiated alloys at least for the Fe-15 at.% Cr. The most obvious conclusion is that existing segregation at grain boundaries in the more concentrated alloys is not greatly affected by irradiation, possibly except for forming a W profile at the Σ5 boundary. However, even this conclusion is confounded by the presence of boundary carbide and nitride phases, which take up Cr leading to local depletion as observed in the classical heat treatment sensitization effect [72]. The grain boundary precipitates may cause further depletion by consuming Cr in a way that may be promoted by radiation-enhanced diffusion. An absence of RIS would suggest that there is no bias associated with the diffusion of Cr by either interstitials or vacancies.

The W-shape profile has been observed in similar alloys after ion and neutron irradiation [1, 73]. W-profiles have been observed in some irradiated austenitic stainless steels with initial Cr segregation before irradiation [68, 74]. It has been hypothesized that these profiles are associated with an intermediate stage of irradiation induced Cr depletion near grain boundaries, that were initially thermally enriched, but are subsequently depleted, following a model developed by Nastar [75]. However it remains unclear as whether these could have also been affected by nearby carbide particles. On the other hand, no Cr-depleted zone is observed around the Σ3 boundary. In the event of a RIS mechanism, it is expected that this interface would be less affected by irradiation due to its limited free volume and sink efficiency. That is, even if Cr diffusion is globally biased, this particular boundary may be more immune to RIS, as was previously observed under ion irradiation [73]. Further, the

unsymmetrical profile of Cr shown in **Fig. 5(a)** might relate to the migration of the $\Sigma 3$ grain boundary under irradiation [76].

Impurities

The same question pertains to the responsible mechanism controlling the segregation behavior of the various impurity elements, notably, P, Si, and C that are all expected to strongly thermally segregate to grain boundaries, given their large segregation enthalpy of order 30, 15 and 50 kJ/mol respectively [66]. Indeed there is a large literature on thermal segregation of these elements [66], including the corresponding consequences to phenomena such as temper embrittlement. Simple thermal segregation calculations are approximately consistent with observed grain boundary solute enrichments in the irradiated condition; indeed, in the case of P the simple models predict even higher concentrations than observed in this study. However, thermal segregation depends on kinetics, as well as thermodynamics, hence on the entire alloy time-temperature history and solute diffusion properties [77-79]; and only interstitial C is expected to be fully equilibrated. Further, thermal non-equilibrium segregation (TNES), due to flow of excess quenched-in vacancies to boundaries, may also occur [80] along with other complications not treated in simple pure binary alloy Langmuir-McLean type models [66]. Thus further discussion of RIS versus RED segregation mechanisms for Cr, P and Si is beyond the scope of this paper. However, our hypothesis is that both RIS and RED are likely to be operative, and both must also be considered in a balanced and experimentally informed way.

Loops

As previously discussed in Refs. [81, 82], dislocations can only be observed if decorated by solute atoms. Therefore the analysis of dislocations using APT relies on the assumption all are segregation sites for solute elements making them visible. The segregation is also assumed to lock dislocations in place preventing them from moving under the stresses created during field evaporation. These assumptions are supported by the fact that the measured number density of dislocations is comparable to or larger than the numbers reported in the literature. Using TEM, Matijasevic et al. [83] reported a dislocation density of 2.1 10^{21} /m^3 with an average loop diameter of 10 nm for a Fe-5 at.% Cr irradiated to similar conditions (300 $^{\circ}$C, 1.7 dpa).

Two types of dislocations have generally been reported in neutron irradiated Fe and Fe-Cr alloys: <100> loops lying on {100} planes and ½<111> loops, for which different habit planes have been observed ({111} [84], {110} [84], and {112} [85]). The measured dislocation habit planes would suggest that ½<111> dislocations are formed. This observation is in agreement with the temperature dependence reported by Jenkins et al. [86] for ion implanted Fe-Cr. Note that Matijasevic et al. [83] found both <100> and ½<111> dislocations in a Fe-6Cr alloy irradiated at 300 $^{\circ}$C to 1.7 dpa but did not indicate the relative proportions.

For loops with larger diameter (18-20 nm) Si and Cr are both segregated around the dislocation line whereas for smaller loop (in the range of 8-10 nm) Cr is found on be periphery of the loop with Si residing inside the loop. While it is conceivable that Si being clustered in the center of small loops is a result of trajectory aberrations or migration during field evaporation, the two distinct populations of sizes suggest a different nature for the smaller and larger loops. A change in the elastic strains may cause Si to distribute differently. Cr is only found in the periphery of the loops where the tensile strains are highest in agreement with recent Monte Carlo and molecular dynamics calculations [87].

Impurity clusters

The extremely low levels of Si, Ni and P in the Fe-15 at.% Cr alloy where impurity clusters were observed would seem to exclude a significant thermodynamic driving force for precipitation of the cited impurities, strongly suggesting a radiation-induced segregation (RIS) and radiation-induced precipitation (RIP) mechanisms are operative in this case. Radiation-induced Si-P-Ni-Cr enriched clusters have previously been reported in ferritic–martensitic steels [88, 89]. Notably, the impurity

clusters are apparently not associated with extended irradiation-induced defects, like visible dislocation loops, and are independent of the α′ precipitates. Thus the homogeneous distribution of the impurity clusters is somewhat puzzling, since RIS typically occurs at sinks for mobile point defects, such as loops, network dislocations and grain boundaries [90]. RIS is typically driven by persistent fluxes of defects to the sinks that couple differentially with solutes like Cr and Fe, such as in an inverse Kirkendall effect [91]. Under irradiation either vacancies or self-interstitials, or both, may be the mobile defect species responsible RIS [92]. In the present case, candidate sinks include small sub-nm vacancy cluster formed in cascades, and/or very small interstitial clusters (proto-loops). These defect clusters cannot be detected in the APT datasets and, in any event, could recover in-situ while leaving behind their solute remnants. Once formed the Si-P-Ni-Cr clusters could continue to grow by RIS, since mobile defects would either annihilate, or recombine, at their incoherent or coherent interfaces, respectively [93].

10.1.2. Ion irradiation

Five different chemistry behaviors were observed, independently of grain boundary orientation and location with respect to the irradiation profile:

- Chromium carbonitride precipitates surrounded by grain boundary Cr depletion
- Chromium concentrations saturating at ~ 26-28 at.% Cr – 2 %C
- Slight enrichment where the Cr concentration peak < 25 at.% Cr
- Overall depletion with grain boundary segregation (W-shaped profile)
- Wide grain boundary depletion (V-shaped profile)

Possible mechanisms to consider would be thermal growth of the grain boundary precipitates associated with fast diffusion of Cr along grain boundary (sensitization), irradiation enhanced growth of the precipitate phases, radiation induced segregation or depletion of Cr by point defect/ Cr interactions. At this stage, the exact mechanism(s) is(are) difficult to distinguish. While it is certain that some amount of sensitization is occurring under ion irradiation conditions possibly due to carbon and nitrogen contamination, the contribution from point defect/Cr interactions is less clear.

At 300 $^{\mathrm{o}}$C, with the exception of the grain boundary covered with the carbonitride precipitates, all boundaries showed segregation at the saturation level. We speculate that if irradiation plays a role at this temperature it is more likely to be radiation-induced segregation of Cr similar to what was observed in the neutron irradiated alloys at a similar temperature of 290 $^{\mathrm{o}}$C. The depletion observed in figure 10 is due to a sensitization mechanism.

At 500 $^{\mathrm{o}}$C, Cr depletion is observed without the presence of visible particles – which may have been missed by the analyzed volume. Whether sensitization is accelerated at higher temperature or radiation-induced depletion occurs is still an open question. The issue of volume of analysis and careful particle analysis remains a challenge.

Finally, the amount of carbon segregation at the grain boundaries for all alloys and conditions suggests that the near surface region may experience some level of surface contamination.

11. Summary and conclusions

The following experiments were performed:

- Fe-Cr alloys containing 5, 10 and 15 at.% Cr were subjected to 5 MeV Fe^{++} ion irradiation at 300 and 500 ^{o}C up to 60 dpa at a dose rate of 10^{-4} dpa/s.

- The Fe-15 at.% Cr alloy was subjected to 5 MeV Fe^{++} ion irradiation at 300 ^{o}C to 0.3 dpa at a dose rate of 10^{-6} dpa/s.

- Fe-Cr alloys containing 3, 6, 9, 12, 15, 18 at.% Cr were subjected to neutron irradiation at 290 ^{o}C to 1.6 dpa at a dose rate of 10^{-7} dpa/s. Subsequently the Fe-18 at.% Cr alloy was annealed at 500 and 600 ^{o}C.

The work resulted in the following observations:

- Neutron irradiation leads to α' precipitation in alloys containing > 9 at.% Cr. The number density decreases and size increases with increasing Cr concentration. The measured Cr concentration is > 77 at.% Cr.

- The solubility limit of Cr under neutron irradiation at 300 ^{o}C and dose rate of 10^{-7} dpa/s is 8.9 at.% Cr.

- Upon annealing at 500 ^{o}C, α' precipitates coarsen and the matrix reaches a concentration considered the solubility limit of Cr at 500 ^{o}C under thermal equilibrium condition (13.2 at.%).

- The measured Cr concentration is α' precipitates appear to strongly depend on precipitate size and may reflect a trajectory aberration effect inherent to field evaporation of phases of different evaporation fields.

- Cr and Si segregate to dislocation loops formed during irradiation. However no α' precipitate is observed on loops.

- When present, Si and P also form small clusters in the neutron irradiated alloys.

- A zone free of α' precipitate is observed at grain boundaries.

- Grain boundaries generally exhibit Cr segregation (one exception was noted in the Fe-6 at.% Cr alloys before irradiation). Comparable segregation levels are observed before and after irradiation for all other alloys. Annealing at 500 ^{o}C also leads to Cr segregation. It is therefore unclear whether irradiation enhances segregation.

- Cr depletion observed along grain boundaries in the Fe- 15 at.% Cr alloy is associated with a sensitization effect rather than radiation induced.

- No α' forms during ion irradiation at dose rates of 10^{-4} dpa/s at 300 to 500 ^{o}C for doses between 1 and 60 dpa.

- At 500 ^{o}C, Cr forms a low density of small clusters of different morphologies (spheres, rods, plates) with concentrations between 20 and 50 at.% Cr. The clusters are associated with C segregation and the spatial distribution and morphology of these segregated regions strongly suggested an association with dislocations.

- At 300 ^{o}C, Cr also forms clusters (with an estimated concentration of <20 at.% Cr) on the inside of dislocation loops in the more dilute alloy. Segregation of C is also observed. However, the concentrated alloy does not exhibit a strong clustering behavior.

- In the alloys ion irradiated at 300 ^{o}C, Cr is segregated to grain boundaries.

- At 500 ^{o}C, sensitization due to the relatively high C and N levels complicates the results with both depletion and segregation observed depending on the grain boundary and location along the same boundary.

- A lower dose rate experiment suggest the formation of larger Cr clusters, with a concentration between 40- and 50 at.% Cr.

To conclude, significant differences are observed between neutron and ion irradiated Fe-Cr alloys. Neutron irradiation leads to phase separation in accordance to the Fe-Cr phase diagram. However α' is not observed after high dose rate ion irradiation. Rather Cr clusters are formed with compositions that strongly depend on dose rate and temperature. The ion irradiation experiments are significantly challenged by carbon and nitrogen contamination, which may also affect the behavior of Cr. While Cr segregation to dislocation loops is observed after the neutron and ion irradiations, α' precipitation is generally anti-correlated with dislocation loops, other solute clusters and grain boundaries, suggesting that point defects and Cr interactions and their concentration dependence plays a significant role in phase stability. Further work is in progress to characterize α' in alloy neutron irradiated to high dose and high temperature to clarify the steady state microstructure. Lower dose rate ion irradiation are also in progress to clarify the dose, dose rate, and temperature dependence of α' nucleation.

12. Acknowledgments

13. Publications and Presentations

13.1. Publications

13.1.1. Peer-reviewed journals

- E.A. Marquis, Atom probe tomography applied to the analysis of irradiated microstructures, Journal of Materials Research (invited review) Dec. 2014
- M. Bachhav, G.R. Odette, E.A. Marquis, Microstructural changes in a neutron-irradiated Fe-15at.%Cr alloy, Journal of Nuclear Materials (2014) 454, 381
- M. Bachhav, L. Yao, G.R. Odette, E.A. Marquis, Microstructural changes in a neutron-irradiated Fe-6at.%Cr alloy, Journal of Nuclear Materials (2014) 453, 334
- M. Bachhav, G.R. Odette, E.A. Marquis, α′ precipitation in neutron irradiated Fe-Cr alloys, Scripta Materialia (2014) 74, 48-51
- E.A. Marquis, M. Bachhav, Y. Chen, Y. Dong, L. Gordon, A. McFarland, On the current role of atom probe tomography in materials characterization and materials science, Current opinions in solid state and materials science (2013) 17(5) 217-223
- *AP Selby, A Kohnert, B Ramirez, BD Wirth, Inverse Kirkendall Models of Radiation Induced Segregation in Cascade Damage Conditions In preparation*

13.1.2. Conference proceedings

- M.N. Bachhav, Y. Chen and E.A. Marquis, Measuring Chemical Segregation at Grain Boundaries by Atom Probe Tomography, Microscopy and Microanalysis (2013) 19(S2) 940-941

13.2. Presentations

- E.A. Marquis, Microstructural evolution of materials under irradiation using atom probe tomography, Workshop on Nanomaterials and Engineered Microstructures for Nuclear Applications, Brookhaven National Laboratory, March 2013
- E.A. Marquis, Atomic scale chemistry of interfaces, Seminar, Los Alamos National Laboratory, July 2013
- M.N. Bachhav, Y. Chen and E.A. Marquis, Measuring Chemical Segregation at Grain Boundaries by Atom Probe Tomography, Annual Microscopy and Microanalysis Meeting, August 2013.
- M. Bachhav, G.R. Odette, E.A. Marquis, Clustering and Radiation induced segregation in Neutron irradiated Fe-(3-18)Cr Alloys, Annual Fall MRS meeting, Boston, December 2013
- E.A. Marquis, M.N. Bachhav, R. Mathew, G.R. Odette, Behavior of Fe-Cr alloys under ion or neutron irradiation, Annual TMS Meeting, San Diego, Feb. 2014 (invited presentation)
- M.N. Bachhav, L. Yao, G.R. Odette, E.A. Marquis, Microstructural evolution after neutron irradiation of Fe-Cr alloys, Annual TMS Meeting, Orlando, Feb. 2015 (invited presentation)
- M.N. Bachhav, L. Yao, G.R. Odette, E.A. Marquis, Microstructural evolution after neutron irradiation of Fe-Cr alloys, Annual MRS Spring Meeting, San Francisco, March. 2015
- E.A. Marquis, APT analyses of neutron irradiated alloys and steels, CAES user meeting, June 2015
- E.A. Marquis, APT analyses of ion and neutron irradiated microstructures, irradiation workshop, Oxford, UK, September 2015

- E.A. Marquis, Evolution of irradiated microstructures, Society of Engineering Science (SES) 52nd Annual Technical Meeting, Texas A&M, October 2015
- E.A. Marquis, Workshop on 'Atom Probe Tomography', Indian Institute of Science (IISc), Bangalore, India, February 2016

14. References

[1] E.A. Marquis, R. Hu, T. Rousseau. A systematic approach for the study of radiation-induced segregation/depletion at grain boundaries in steels. **Journal of Nuclear Materials** 413 (**2011**) 1.

[2] D.S. Bae, S.K. Kim, S.P. Lee, H. Kinoshita, T. Shibayama, H. Takahashi. Effect of electron irradiation on microstructural damage in the welded portion of a SUS304 weldment. **Fusion Engineering and Design** 81 (**2006**) 969.

[3] H. Takahashi, S. Ohnuki, T. Takeyama. Radiation-induced segergation at internal sinks in electron-irradiated binary alloys. **Journal of Nuclear Materials** 103 (**1982**) 1415.

[4] Z. Lu, R.G. Faulkner, N. Sakaguchi, H. Kinoshita, H. Takahashi, P.E.J. Flewitt. Effect of hafnium on radiation-induced inter-granular segregation in ferritic steel. **Journal of Nuclear Materials** 351 (**2006**) 155.

[5] E.L. Hall, C.L. Briant. Chromiun depletion in the vicinity of carbides in sensitized austenitic stainless steels. **Metallurgical Transactions A** 15 (**1984**) 793.

[6] A.S.M. Paroni, N. Alonso-Falleiros, R. Magnabosco. Sensitization and pitting corrosion resistance of ferritic stainless steel aged at 800 degrees C. **Corrosion** 62 (**2006**) 1039.

[7] P. Grobner. The 885 F (475 C) embrittlement of ferritic stainless steels. **Metallurgical Transactions** 4 (**1973**) 251.

[8] J.T. Busby, G.S. Was, E.A. Kenik. Isolating the effect of radiation-induced segregation in irradiation-assisted stress corrosion cracking of austenitic stainless steels. **Journal of Nuclear Materials** 302 (**2002**) 20.

[9] S. Hertzman, B. Sundman. A thermodynamic analysis of the Fe-Cr system. **Calphad** 6 (**1982**) 67.

[10] P. Olsson, J. Wallenius, C. Domain, K. Nordlund, L. Malerba. Two-band modeling of alpha-prime phase formation in Fe-Cr. **Physical Review B** 72 (**2005**).

[11] A. Caro, M. Caro, E.M. Lopasso, D.A. Crowson. Implications of ab initio energetics on the thermodynamics of Fe-Cr alloys. **Applied Physics Letters** 89 (**2006**).

[12] G. Bonny, D. Terentyev, L. Malerba. On the alpha-alpha ' miscibility gap of Fe-Cr alloys. **Scripta Materialia** 59 (**2008**) 1193.

[13] D. Nguyen-Manh, M.Y. Lavrentiev, S.L. Dudarev. Ab initio and Monte Carlo modeling in Fe-Cr system: Magnetic origin of anomalous thermodynamic and kinetic properties. **Computational Materials Science** 44 (**2008**) 1.

[14] J. Cermak, J. Ruzickova, A. Pokorna. Low-temperature tracer diffusion of chromium in Fe-Cr ferritic alloys. **Scripta Materialia** 35 (**1996**) 411.

[15] A. Bowen, G. Leak. Solute diffusion in alpha-and gamma-iron. **Metallurgical Transactions** 1 (**1970**) 1695.

[16] W. Xiong, M. Selleby, Q. Chen, J. Odqvist, Y. Du. Phase Equilibria and Thermodynamic Properties in the Fe-Cr System. **Critical Reviews in Solid State and Materials Sciences** 35 (**2010**) 125.

[17] M.H. Mathon, Y. De Carlan, G. Geoffroy, X. Averty, A. Alamo, C.H. De Novion. A SANS investigation of the irradiation-enhanced α-α′ phases separation in 7-12 Cr martensitic steels. **Journal of Nuclear Materials** 312 (**2003**) 236.

[18]   A. Kimura, H. Matsui. Neutron irradiation effects on the microstructure of low-activation ferritic alloys. **Journal of Nuclear Materials** 212-215 (**1994**) 701.

[19]   E.A. Little, D.A. Stow. VOID-SWELLING IN IRONS AND FERRITIC STEELS .2. EXPERIMENTAL SURVEY OF MATERIALS IRRADIATED IN A FAST-REACTOR. **Journal of Nuclear Materials** 87 (**1979**) 25.

[20]   Y.V. Konobeev, A.M. Dvoriashin, S.I. Porollo, F.A. Garner. Swelling and microstructure of pure Fe and Fe-Cr alloys after neutron irradiation to similar to 26 dpa at 400 degrees C. **Journal of Nuclear Materials** 355 (**2006**) 124.

[21]   F. Bergner, A. Ulbricht, C. Heintze. Estimation of the solubility limit of Cr in Fe at 300 °C from small-angle neutron scattering in neutron-irradiated Fe–Cr alloys. **Scripta Materialia** 61 (**2009**) 1060.

[22]   H. Kuwano, Y. Yamaguchi. MoSSBAUER STUDY OF IRON-CHROMIUM ALLOYS IRRADIATED BY ENERGETIC PROTONS. **Journal of Nuclear Materials** 155-157 (**1988**) 1071.

[23]   Z. Jiao, G.S. Was. Novel features of radiation-induced segregation and radiation-induced precipitation in austenitic stainless steels. **Acta Materialia** 59 (**2011**) 1220.

[24]   C.D. Hardie, C.A. Williams, S. Xu, S.G. Roberts. Effects of Irradiation Temperature and

Dose Rate on the Mechanical Properties of Self-Ion Implanted Fe and Fe-Cr Alloys,. **Journal of Nuclear Materials** 439 (**2013**) 33.

[25]   A. Bhattacharya, E. Meslin, J. Henry, C. Pareige, B. Décamps, C. Genevois, D. Brimbal, A. Barbu. Chromium enrichment on the habit plane of dislocation loops in ion-irradiated high-purity Fe–Cr alloys. **Acta Materialia** 78 (**2014**) 394.

[26]   J.-J. Kai, G.L. Kulcinski, R.A. Dodd. Effects of Heavy-Ion Irradiation on HT-9 Ferritic Steel Examined in Cross Section. In: Garner FA, Packan NH, Kumar AS, editors. Radiation-Induced Changes in Microstructure: 13th International Symposium {Part I), ASTM STP 955: American Society for Testing and Materials, Philadelphia,, 1987. p.530.

[27]   O.V. Borodin, V.N. Voyevodin, V.D. Zelensky, I.M. Neklyudov, P.V. Platonov. Radiation Damage Studies of the I0 to 13% Chromium-Containing Steels and Alloys Irradiated with Heavy Ions. In: Stoller RE, Kumar AS, Gelles DS, editors. Effects of Radiation on Materials. 15 th International Symposium, ASTMSTP 1125: American Society for Testing and Materials, Philadelphia, 1992. p.1157.

[28]   T.R. Allen, L. Tan, J. Gan, G. Gupta, G.S. Was, E.A. Kenik, S. Shutthanandan, S. Thevuthasan. Microstructural development in advanced ferritic-martensitic steel HCM12A. **Journal of Nuclear Materials** 351 (**2006**) 174.

[29]   R.E. Clausing, L. Heatherly, R.G. Faulkner, A.F. Rowcliffe, K. Farrell. Radiatio ninduced segregation in HT-9 martensitic steel **Journal of Nuclear Materials** 141 (**1986**) 978.

[30]   R.G. Faulkner, R.B. Jones, Z. Lu, P.E.J. Flewitt. Grain boundary impurity segregation and neutron irradiation effects in ferritic alloys. **Philosophical Magazine** 85 (**2005**) 2065.

[31]   G. Gupta, Z. Jiao, A.N. Ham, J.T. Busby, G.S. Was. Microstructural evolution of proton irradiated T91. **Journal of Nuclear Materials** 351 (**2006**) 162.

[32]   T. Kato, H. Takahashi, S. Ohnuki, K. Nakata, J. Kuniya. The effect of solute content on grain boundary segregation in electron irradiated Fe-Cr-mn alloys. **Journal of Nuclear Materials** 179 (**1991**) 623.

[33]   Z. Lu, R.G. Faulkner, G. Was, B.D. Wirth. Irradiation-induced grain boundary chromium microchemistry in high alloy ferritic steels. **Scripta Materialia** 58 (**2008**) 878.

[34]   S. Ohnuki, H. Takahashi, T. Takeyama. Vois swelling and segregation of solute in ion irradiated ferritic steels. **Journal of Nuclear Materials** 103 (**1982**) 1121.

[35]   R. Schaublin, P. Spatig, M. Victoria. Chemical segregation behavior of the low activation ferritic/martensitic steel F82H. **Journal of Nuclear Materials** 258 (**1998**) 1350.

[36]   M.J. Hackett, J.T. Busby, M.K. Miller, G.S. Was. Effects of oversized solutes on radiation-induced segregation in austenitic stainless steels. **Journal of Nuclear Materials** 389 (**2009**) 265.

[37]   D.S. Gelles. MICROSTRUCTURAL EXAMINATION OF NEUTRON-IRRADIATED SIMPLE FERRITIC ALLOYS. **Journal of Nuclear Materials** 108 (**1982**) 515.

[38]   D.S. Gelles. VOID SWELLING IN BINARY FE-CR ALLOYS AT 200 DPA. 17th International Symposium on the Effects of Radiation on Materials. Sun Valley, Id, 1994. p.163.

[39]   J.J. Penisten. The Mechanism of Radiation-Induced Segregation in Ferritic-Martensitic Steels. The University of Michigan, 2012.

[40]   J. Ziegler. SRIM - Stopping Ranges of Ions in Matter. 2008.

[41]   N. Juslin, K. Nordlund, J. Wallenius, L. Malerba. Simulation of threshold displacement energies in FeCr. **Nuclear Instruments and Methods in Physics Research Section B: Beam Interactions with Materials and Atoms,** 255 (**2007**) 75.

[42]   S.I. Porollo, A.N. Vorobjev, Y.V. Konobeev, A.M. Dvoriashin, V.M. Krigan, N.I. Budylkin, E.G. Mironova, F.A. Garner. Swelling and void-induced embrittlement of austenitic stainless steel irradiated to 73-82 dpa at 335-365 degrees C. **Journal of Nuclear Materials** 258 (**1998**) 1613.

[43]   K. Thompson, D. Lawrence, D.J. Larson, J.D. Olson, T.F. Kelly, B. Gorman. In situ site-specific specimen preparation for atom probe tomography. **Ultramicroscopy** 107 (**2007**) 131.

[44]   M.K. Miller, M.G. Hetherington. Local magnification effects in the atom probe. **Surface Science** 246 (**1991**) 442.

[45]   E.A. Marquis, B.P. Geiser, T.J. Prosa, D.J. Larson. Evolution of tip shape during field evaporation of complex multilayer structures. **Journal of Microscopy** 241 (**2011**) 225.

[46]   L.T. Stephenson, M.P. Moody, P.V. Liddicoat, S.P. Ringer. New techniques for the analysis of fine-scaled clustering phenomena within atom probe tomography (APT) data. **Microscopy and Microanalysis** 13 (**2007**) 448.

[47]   E.A. Marquis, J.M. Hyde. Applications of atom-probe tomography to the characterisation of solute behaviours. **Materials Science & Engineering R-Reports** 69 (**2010**) 37.

[48]   D. Vaumousse, A. Cerezo, P.J. Warren. A procedure for quantification of precipitate microstructures from three-dimensional atom probe data. **Ultramicroscopy** 95 (**2003**) 215.

[49]   A. Cerezo, L. Davin. Aspects of the observation of clusters in the 3-dimensional atom probe. **Surface and Interface Analysis** 39 (**2007**) 184.

[50]   F. Vurpillot, A. Bostel, D. Blavette. Trajectory overlaps and local magnification in three-dimensional atom probe. **Applied Physics Letters** 76 (**2000**) 3127.

[51]   E.A. Marquis, F. Vurpillot. Chromatic aberrations in the field evaporation behavior of small precipitates. **Microscopy and Microanalysis** 14 (**2008**) 561.

[52]   A. Morley, G. Sha, S. Hirosawa, A. Cerezo, G.D.W. Smith. Determining the composition of small features in atom probe: bcc Cu-rich precipitates in an Fe-rich matrix. **Ultramicroscopy** 109 (**2009**) 535.

[53]   D.R. Kingham. Model calculations of tunnelling and thermal evaporation rate constants relating to field evaporation. **J. Phys. D: Appl. Phys.** 15 (**1982**) 2537.

[54]   O.C. Hellman, J.A. Vandenbroucke, J. Rüsing, D. Isheim, D.N. Seidman. Analysis of three-dimensional atomprobe data by the proximity histogram. **Microscopy and Microanalysis** 6 (**2000**) 437.

[55]   R.P. Kolli, D.N. Seidman. Comparison of Compositional and Morphological Atom-Probe Tomography Analyses for a Multicomponent Fe-Cu Steel. **Microscopy and Microanalysis** 13 (**2007**) 272.

[56]   J.M. Titchmarsh, S. Dumbill. On the measurement of radiation-induced segregation (RIS) point defect sinks. **J. Nucl. Mater** 227 (**1996**) 203.

[57]   M. Bachhav, Y. Chen, E.A. Marquis, B. Geiser. Measuring Chemical Segregation at Grain Boundaries by Atom Probe Tomography. **Microscopy and Microanalysis** 19 (**2013**) 940.

[58]   B.W. Krakauer, D.N. Seidman. Absolute atormis scale measurements of the Gibbsian interfacial excess of solute at internal interfaces. **Physical Review B** 49 (**1993**) 6724.

[59]   E. Martínez, O. Senninger, C.-C. Fu, F. Soisson. Decomposition kinetics of Fe-Cr solid solutions during thermal aging. **Physical Review B** 86 (**2012**) 224109.

[60]   G. Bonny, D. Terentyev, L. Malerba. On the α–α′ miscibility gap of Fe–Cr alloys. **Scripta Materialia** 59 (**2008**) 1193.

[61]   V. Kuksenko, C. Pareige, P. Pareige. Cr precipitation in neutron irradiated industrial purity Fe–Cr model alloys. **Journal of Nuclear Materials** 432 (**2013**) 160.

[62]   D.S. Gelles, R.E. Schaublin. Post-irradiation deformation in a Fe-9%Cr alloy. **Dislocations 2000: An International Conference on the Fundamentals of Plastic Deformation** 309-310 (**2001**) 82

[63]   S. Novy, P. Pareige, C. Pareige. Atomic scale analysis and phase separation understanding in a thermally aged Fe–20 at.%Cr alloy. **Journal of Nuclear Materials** 384 (**2009**) 96.

[64]   M.L. Jenkins, Z. Yao, M. Hernandez-Mayoral, M.A. Kirk. Dynamic observations of heavy-ion damage in Fe and Fe-Cr alloys. **Journal of Nuclear Materials** 389 (**2009**) 197.

[65]   Z. Balogh, P. Stender, M.R. Chellali, G. Schmitz. Investigation of Interfaces by Atom Probe Tomography. **Metallurgical and Materials Transactions A,** (**2012**) 1.

[66]   P. Lejček. Grain boundary segregation in metals: Springer, **2010**.

[67]   S. Watanabe, Y. Takamatsu, N. Sakaguchi, H. Takahashi. Sink effect of grain boundary on radiation-induced segregation in austenitic stainless steel. **Journal of Nuclear Materials** 283–287, Part 1 (**2000**) 152.

[68]   E.A. Kenik, J.T. Busby, M.K. Miller, A.M. Thuvander, G. Was. Origin and Influence of Pre-Existing Segregation On Radiation-Induced Segregation in Austenitic Stainless Steels. **MRS Proceedings** 540 (**1998**).

[69]   R. Schäublin, P. Spätig, M. Victoria. Chemical segregation behavior of the low activation ferritic/martensitic steel F82H. **Journal of Nuclear Materials** 258–263, Part 2 (**1998**) 1350.

[70]   T.R. Anthony. SOLUTE SEGREGATION IN VACANCY GRADIENTS GENERATED BY SINTERING AND TEMPERATURE CHANGES. **Acta Metallurgica** 17 (**1969**) 603.

[71]   R.G. Faulkner. COMBINED GRAIN-BOUNDARY EQUILIBRIUM AND NONEQUILIBRIUM SEGREGATION IN FERRITIC MARTENSITIC STEELS. **Acta Metallurgica** 35 (**1987**) 2905.

[72]   T.S. Duh, J.J. Kai, F.R. Chen. Effects of grain boundary misorientation on solute segregation in thermally sensitized and proton-irradiated 304 stainless steel. **Journal of Nuclear Materials** 283 (**2000**) 198.

[73]   R. Hu, G.D.W. Smith, E.A. Marquis. Effect of Grain Boundary Orientation on Radiation-Induced Segregation in a Fe-15.2 at%Cr Alloy. **Acta Materialia** (**2013**).

[74]   C.C. Goodwin, R.G. Faulkner, S.B. Fisher. The Modelling of Combined Radiation-Induced and Thermal Non-Equilibrium Segregation of Chromium in Neutron-Irradiated Austenitic Stainless Steels. **ASTM SPECIAL TECHNICAL PUBLICATION** 1325 (**1999**) 634.

[75]   M. Nastar. Segregation at grain boundaries: from equilibrium to irradiation induced steady states. **Philosophical Magazine** 85 (**2005**) 641.

[76]   S. Watanabe, N. Sakaguchi, N. Hashimoto, H. Takahashi. Quantitative studies of irradiation-induced segregation and grain boundary migration in FeCrNi alloy. **Journal of Nuclear Materials** 224 (**1995**) 158.

[77]   T. Matsuyama, H. H., S. Hajime. Tracer diffusion of P in iron and iron alloys. **Transactions of the Japan institute of metals** 24 (**1983**) 589.

[78]   R.J. Borg, D.Y.F. Lai. Diffusion in α-Fe–Si Alloys. **Journal of Applied Physics** 41 (**1970**) 5193.

[79]   K.E. Blazek, J.R. Cost. Carbon diffusivity in iron-chromium alloys. **Transactions of the Japan Institute of Metals** 17 (**1976**) 630.

[80]   T.R. Anthony, R.E. Hanneman. NON-EQUILIBRIUM SEGREGATION OF IMPURITIES IN QUENCHED DILUTE ALLOYS. **Scripta Metallurgica** 2 (**1968**) 611.

[81]   M.K. Miller. Atom probe tomography characterization of solute segregation to dislocations. **Microscopy Research and Technique** 69 (**2006**) 359.

[82]   C.A. Williams, J.M. Hyde, G.D.W. Smith, E.A. Marquis. Effects of heavy-ion irradiation on solute segregation to dislocations in oxide-dispersion-strengthened Eurofer 97 steel. - 412 (**2011**).

[83]   M. Matijasevic, A. Almazouzi. Effect of Cr on the mechanical properties and microstructure of Fe–Cr model alloys after n-irradiation. **Journal of Nuclear Materials** 377 (**2008**) 147.

[84]   S.J. Zinkle, B.N. Singh. Microstructure of neutron-irradiated iron before and after tensile deformation. **Journal of Nuclear Materials** 351 (**2006**) 269.

[85]   J. Chen, N. Gao, P. Jung, T. Sauvage. A new mechanism of loop formation and transformation in bcc iron without dislocation reaction. **Journal of Nuclear Materials** 441 (**2013**) 216.

[86]   M. Jenkins, Z. Yao, M. Hernandez-Mayoral, M. Kirk. Dynamic observations of heavy-ion damage in Fe and Fe–Cr alloys. **Journal of Nuclear Materials** 389 (**2009**) 197.

[87]   D. Terentyev, F. Bergner, Y. Osetsky. Cr segregation on dislocation loops enhances hardening in ferritic Fe–Cr alloys. **Acta Materialia** 61 (**2013**) 1444.

[88]   P.J. Maziasz. Formation and stability of radiation-induced phases in neutron-irradiated austenitic and ferritic steels. **Journal of Nuclear Materials** 169 (**1989**) 95.

[89]   R.G. Faulkner, E.A. Little, T.S. Morgan. Irradiation inducved grain and lath boundary segregation in ferritic martensitic steels. **Journal of Nuclear Materials** 191 (**1992**) 858.

[90]   A.J. Ardell. RADIATION-INDUCED SOLUTE SEGREGATION IN ALLOYS. **Materials Issues for Generation IV Systems** (**2008**) 285.

[91]   A.D. Marwick. Segregation in irradiated alloys : The inverse Kirkendall effect and the effect of constitution on void swelling. **J. Phys. F: Metal Phys.** 8 (**1978**) 1849.

[92]   H. Wiedersich, P.R. Okamoto, N.Q. Lam. THEORY OF RADIATION-INDUCED SEGREGATION IN CONCENTRATED ALLOYS. **Journal of Nuclear Materials** 83 (**1979**) 98.

[93]   A. Barbu, A.J. Ardell. Irradiation-induced precipitation in Ni-Si alloys. **Scripta Metall.** 9 (**1975**) 1233.